MJO-Induced Warm Pool Eastward Extension Prior to the Onset of El Niño: Observations from 1998 to 2019

YAKELYN R. JAUREGUI[a] AND SHUYI S. CHEN[a]

[a] *Department of Atmospheric Sciences, University of Washington, Seattle, Washington*

(Manuscript received 19 April 2023, in final form 31 October 2023, accepted 1 November 2023)

ABSTRACT: The Madden–Julian oscillation (MJO) and El Niño–Southern Oscillation (ENSO) are the two most important tropical phenomena that affect global weather and climate on intraseasonal and interannual time scales. Although they occur on different time scales, the MJO-induced sea surface temperature (SST) anomalies over the equatorial Pacific have spatial scales similar to SST anomalies prior to El Niño. This study aims to address the question of whether the MJO plays an important role in the warm pool eastward extension (WPEE) leading up to El Niño. We use over 20 years of satellite observations, including optimum interpolated SST, TRMM-GPM precipitation, and the cross-calibrated multiplatform (CCMP) surface winds from 1998 to 2019, to quantify the spatial structure and duration of the MJO-induced warm SST anomalies over the equatorial Pacific (10°S–10°N, 130°E–180°). The intensity of the MJO is measured by the total rain volume and average surface westerly wind speed throughout its convectively active phase. Results show that 1) 61% of the 98 MJO events induced a WPEE over 1000–3000 km along the equator, which can last beyond 15–30 days after the MJO precipitation ended; 2) the MJO events prior to El Niño are generally stronger and produce significant WPEE far beyond its annual cycle and increasing SST warming in the Niño-3.4 region; 3) consecutive MJO events can produce much stronger WPEE prior to El Niño, which are observed in all El Niño events from 1998 to 2019; and 4) more frequent and stronger MJO-induced WPEE occurs in March–May than other seasons. These results can help better understand the MJO–ENSO interaction and, ultimately, improve the prediction of El Niño onset.

KEYWORDS: ENSO; Madden-Julian oscillation; Sea surface temperature; Warm pool; Wind bursts

1. Introduction

El Niño–Southern Oscillation (ENSO) is the predominant mode of interannual (2–7 years) variability that exerts a profound influence on the global weather and climate (Philander et al. 1984). ENSO manifests as alternating periods of anomalously warm and cold ocean conditions in the Pacific, characterized by variability in amplitude, duration, and temporal and spatial structures (Capotondi et al. 2015). One of the most challenging aspects of ENSO prediction is the onset of El Niño (McPhaden et al. 2006a; Guilyardi et al. 2009; McPhaden 2015; L'Heureux et al. 2017), which is marked by an initial warming of the upper ocean across the Pacific (Kessler 2002). This initial warming occurs when the west Pacific warm pool is extended eastward beyond its climatological position.

The Madden–Julian oscillation (MJO) (Madden and Julian 1971, 1972) occurs on intraseasonal time scales (~30–90 days) with anomalous large-scale precipitation and zonal winds propagating from the tropical Indian Ocean to the west-central Pacific (Zhang 2005, 2013). Although the MJO and ENSO occur on different time scales, they can interact, especially over the tropical Pacific (Kessler and Kleeman 2000; Bergman et al. 2001; Lengaigne et al. 2002). Both observations (Lau and Chan 1988; Kessler et al. 1995; Zhang and Gottschalck 2002; Maes et al. 2002, 2006; Bosc et al. 2009) and modeling studies (McPhaden and Yu 1999; Kessler and Kleeman 2000; Suzuki and Takeuchi 2000; Lengaigne et al. 2002, 2003) have suggested that the MJO may contribute to the onset of El Niño through various processes. Zhang et al. (2001) provided a summary of the MJO–ENSO interaction based on a workshop on this topic.

The displacement of the west Pacific warm pool's eastern edge has been studied on intraseasonal (Kessler et al. 1995; Drushka et al. 2015) and interannual time scales (Delcroix and Hénin 1991; Picaut et al. 1997; Vialard and Delecluse 1998; Maes et al. 2002, 2005; Maes and Belamari 2011; Singh and Delcroix 2013). Kessler et al. (1995) proposed that westerly wind bursts (WWBs), particularly those associated with the MJO, play a crucial role in generating intraseasonal oceanic Kelvin waves and promoting the warm pool eastward extension (WPEE) on intraseasonal time scales. Several studies have emphasized the significance of the eastward advection of warm water by geostrophic currents induced by wind-forced downwelling Kelvin waves (Kessler et al. 1995; Picaut and Delcroix 1995; McPhaden 1999; Lengaigne et al. 2002; Zhang and Gottschalck 2002). However, Kessler et al. (1995) also pointed out that abrupt shifts in the warm pool's eastern edge are not always associated with Kelvin waves. Using the traditional MJO RMM index (Wheeler and Hendon 2004), Drushka et al. (2015) did not find a clear association between the WPEE and various MJO phases identified by RMM. It is not surprising, given that the RMM index is based on EOF analysis of the OLR and tropospheric wind anomalies, which are not directly connected with the actual surface forcing of the ocean from the MJO and, therefore, may not be correlated with the ocean response.

To understand the relationship between the WPEE and the MJO, observational studies of oceanic processes associated with the MJO, specifically the ocean response to MJO forcing through westerly winds and freshwater from the MJO precipitation,

Corresponding author: Yakelyn R. Jauregui, yakelynr@uw.edu

DOI: 10.1175/JCLI-D-23-0234.1

© 2024 American Meteorological Society. This published article is licensed under the terms of the default AMS reuse license. For information regarding reuse of this content and general copyright information, consult the AMS Copyright Policy (www.ametsoc.org/PUBSReuseLicenses).

Brought to you by NOAA Central Library | Unauthenticated | Downloaded 08/13/24 07:09 PM UTC

provide direct connections with plausible physical mechanisms. First, Kessler et al. (1995) proposed that MJO-induced westerly winds excite equatorial downwelling Kelvin waves that deepen the thermocline and facilitate the advection of warm waters to the east. This mechanism can play a crucial role in the WPEE. Chiodi et al. (2014) showed that MJO events with WWBs can induce warming up to 0.6°C in the eastern Pacific within 20–80 days, whereas non-WWB events do not significantly affect SST changes. Second, Anderson et al. (1996) showed that the freshwater from the MJO precipitation during convectively phase reduces the density of the ocean surface layer and produces a shallower mixed layer (ML) above the upper-ocean barrier layer (BL), as described by Lukas and Lindstrom (1991). After the MJO deep convection (i.e., during the post-MJO suppressed phase with calm wind and clear-sky conditions), the BL acts as a barrier preventing the intrusion of cold thermocline water into the ML. The presence of a shallower ML and a sufficiently thick BL enables the maximum warming of the upper ocean by retaining a significant portion of shortwave radiation, thereby reinforcing the initial stratification (Anderson et al. 1996; Vialard and Delecluse 1998; Maes et al. 2002, 2006). The penetration of shortwave radiation through the base of the ML plays a vital role in accumulating heat content above the thermocline, which is a precondition for the onset of El Niño (e.g., McPhaden 2012). Furthermore, observational and modeling studies of the MJO have shown that the MJO large-scale convective envelope consists of organized mesoscale convective systems (MCSs; Chen et al. 1996) that can enhance surface westerly winds through the downward transport of momentum into the atmospheric boundary layer (Houze et al. 2000; Mechem et al. 2006). The combination of the two dynamics and thermodynamics physical mechanisms associated with the MJO westerly winds and large-scale precipitation can induce a WPEE during the suppressed phase of the MJO, namely the post-MJO phase (after the convective period).

The direct impacts of MJO-induced westerlies and precipitation/freshwater on the ocean observed by previous studies have been further tested and quantified by a high-resolution coupled atmosphere–ocean modeling study by Kerns and Chen (2021). They found that the effect of the MJO on WPEE is through direct coupling of precipitation, salinity, and wind using coupled model experiments with and without the input of the freshwater from the MJO events prior to the onset of El Niño in 2018.

To further investigate the direct MJO impacts on the ocean surface and WPEE, we expand previous case studies using observations from 1998 to 2019 in this study. We use both precipitation and surface wind observations over a long period with a significant number of MJO events. To quantify the direct impacts of the MJO on the ocean surface temperature in this study, we use the MJO large-scale precipitation tracking (LPT) method originally developed by Kerns and Chen (2016) and further improved with extended observations by Kerns and Chen (2020). In contrast to previous studies using the RMM index based on anomalies, the LPT method enables us to track the actual MJO precipitation and surface westerly winds directly in time and space. It made it possible to investigate the impacts of the MJO on oceanic processes that can provide new insights related to the WPEE. In this study, we analyze nearly 100 MJO events identified using over 20 years of comprehensive multisatellite precipitation data (Kerns and Chen 2020) along with surface wind and SST observations to quantitatively analyze the MJO-induced WPEE over the western Pacific. For simplicity, we refer to the convectively suppressed phase after the active phase as post-MJO for the rest of this paper. We assess the spatial structure and duration of the MJO and the post-MJO WPEE for individual and consecutive MJO events in relation to the six El Niño events from 1998 to 2019.

The remainder of this paper is organized as the following: section 2 describes the observational datasets and the methods used in this study to quantify the duration and intensity of each MJO event and the post-MJO WPEE. To demonstrate the connection between enhanced MJO activity, post-MJO WPEE, and El Niño onset, section 3 presents two specific examples of the MJO events before El Niño 2002 and 2018. Section 4 provides comprehensive analyses of all MJO events observed during 1998–2019, including statistics of MJO-induced WPEE in time and space as well as a composite of warming due to the MJO over the tropical western Pacific. Section 5 further demonstrates that the WPEE is a robust signal above seasonal variability by removing the annual cycle of the warm pool. Section 6 examines the MJO intensity in relation to the WPEE. A summary and conclusions are given in section 7.

2. Data and methods

a. *Precipitation, wind, and SST data*

The Tropical Rainfall Measuring Mission (TRMM) Multisatellite Precipitation Analysis (TMPA) 3B43 V7 data from June 1998 to June 2019 are used to identify the MJO event (Kerns and Chen 2016, 2020). TMPA estimates instantaneous rain rates at 3-hourly intervals on a regular 0.25° grid based on passive-microwave and infrared retrievals (Huffman et al. 2007).

The Cross-Calibrated Multi-Platform version 2 (CCMP V2) wind at 10 m is used to characterize the surface wind associated with the MJO events from June 1998 to June 2019. The 6-hourly and 0.25°-resolution CCMP V2 wind product is produced by Remote Sensing Systems (REMSS) (Atlas et al. 2008). It combines surface wind data from satellite radiometer retrievals, QuikSCAT and ASCAT satellite scatterometer measurements, moored buoys, and ERA-Interim reanalysis using a variational analysis method.

The daily SST data used in this study are from the National Ocean Atmospheric Administration (NOAA) Optimum Interpolation Sea Surface Temperature version 2 (OISST-V2; Reynolds et al. 2002, 2007) at 0.25° spatial resolution. The Niño-3.4 (5°S–5°N, 170°E–120°W) SST monthly anomalies and Oceanic Niño Index (ONI) are obtained from the NOAA Climate Prediction Center (CPC) for real-time ENSO monitoring indexes.

b. *MJO identification*

The MJO events are identified based on the large-scale precipitation tracking (LPT) algorithm developed by Kerns and Chen (2016, 2020) using TMPA data. This method explicitly identifies the evolution of individual MJO events in time and

Brought to you by NOAA Central Library | Unauthenticated | Downloaded 08/13/24 07:09 PM UTC

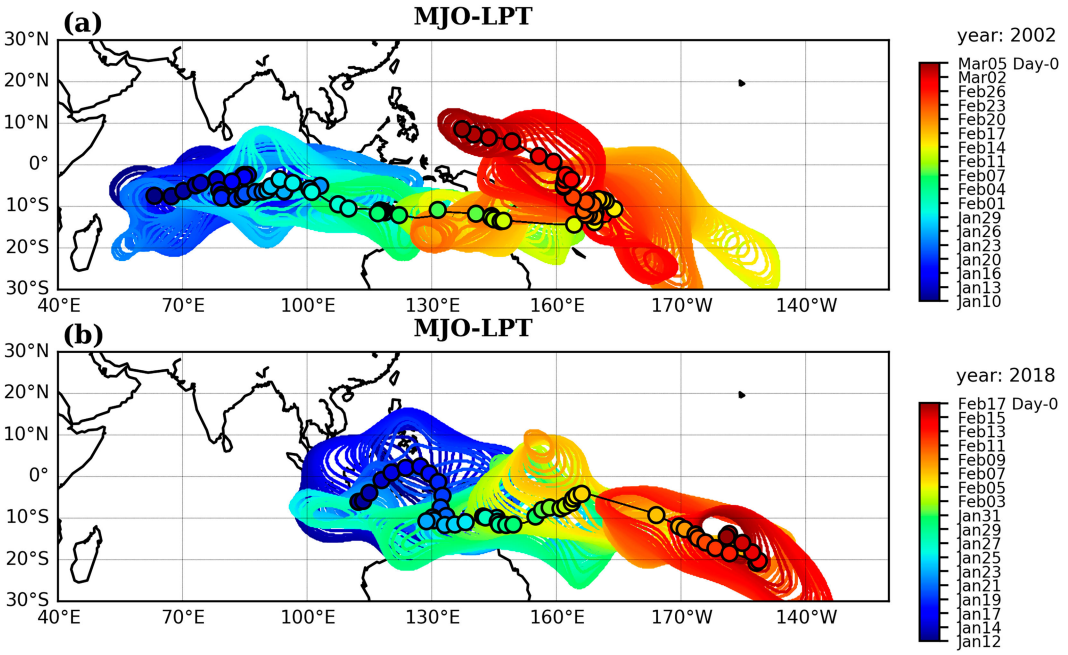

FIG. 1. MJO large-scale precipitation tracking systems (LPTs) shown in color contours evolving in time at 6-hourly intervals for two MJO events: (a) January–March 2002 and (b) January–February 2018. The centroids of the MJO LPT are shown as black circles. The MJO LPT uses 12 mm day^{-1} threshold of the 3-hourly data as described in Kerns and Chen (2020). Day-0 corresponds to the ending date of the MJO-LPTs and the start of the post-MJO-precipitation-phase analysis.

space. A large-scale precipitation object (LPO) is first identified by 12 mm day^{-1} threshold contour using a 5° × 5° spatial filter on the 3-day precipitation accumulation. The LPO is then tracked in time at 3-hourly intervals as an LPT system (LPTs). The MJO LPTs is defined as an LPT system that lasts beyond 10 days with eastward propagation speed > 0 m s^{-1} as described in Kerns and Chen (2020). This LPT method provides the size and intensity of the MJO large-scale convection/precipitation, its center location, structures in both zonal and meridional directions, as well as the starting and ending dates of the MJO precipitation, which are not explicitly represented by the RMM index (Wheeler and Hendon 2004). It is uniquely suited for studying the direct impacts of the MJO on ocean and air–sea interaction. The MJO LPTs database is extended to include 2019 in this study using the same methodology.

Two examples of the MJO LPTs from January–March 2002 and January–February 2018 are shown in Figs. 1a and 1b, respectively. For simplicity, we will use the MJO LPTs and MJO events interchangeably. The 2002 MJO event lasted about 50 days and propagated from the Indian Ocean to the western Pacific with an average eastward speed of 1.7 m s^{-1}, while the 2018 MJO event lasted for 36 days at 3.1 m s^{-1}. We use the centroid and area coverage of the precipitation as represented by a large-scale precipitation object (LPO; defined in Kerns and Chen 2016) that can be tracked in time and space for each MJO event that has a starting and ending time as shown by the color contours in Fig. 1. For simplicity, we refer to the MJO LPT events as the MJO events in this study thereafter.

It is important to note that the MJO precipitation and westerly winds impact the ocean not only during the convective active phase but, more importantly, the long-lasting effects persist during the post-MJO suppressed phase over the equatorial Pacific as shown in previous studies. To investigate the post-MJO WPEE over the tropical west-central Pacific, we selected a subset of the MJO events located within the region of 10°S–10°N, 130°–180°E. Although these MJO events can start and/or end outside of this region, they need to last beyond days within this region. In fact, most of the MJO events in this subset were initiated over the Indian Ocean and propagated eastward across the Maritime Continent to the west-central Pacific. This subset includes 98 MJO events out of a total of more than 200 MJO events from 1998 to 2019. The characteristics of this subset of the MJO and post-MJO WPEE will be compared with overall MJO events.

c. *MJO intensity measured by precipitation and wind*

The MJO, by definition, refers to large-scale convection and circulation patterns that exhibit variability on the intraseasonal time scale (~30–90 days), with convectively active and suppressed phases as they propagate eastward (Madden and Julian 1971, 1972; Zhang 2005). It has been noted by many observational studies that the MJO consists of irregular, anomalous large-scale convection/precipitation that initiate over the Indian Ocean and propagate eastward up to west-central Pacific (e.g., Rui and Wang 1990; Hendon et al. 1998; Kerns and Chen 2020). During the convectively active (suppressed) phase, strong surface westerly (easterly) winds are associated with the MJO

Brought to you by NOAA Central Library | Unauthenticated | Downloaded 08/13/24 07:09 PM UTC

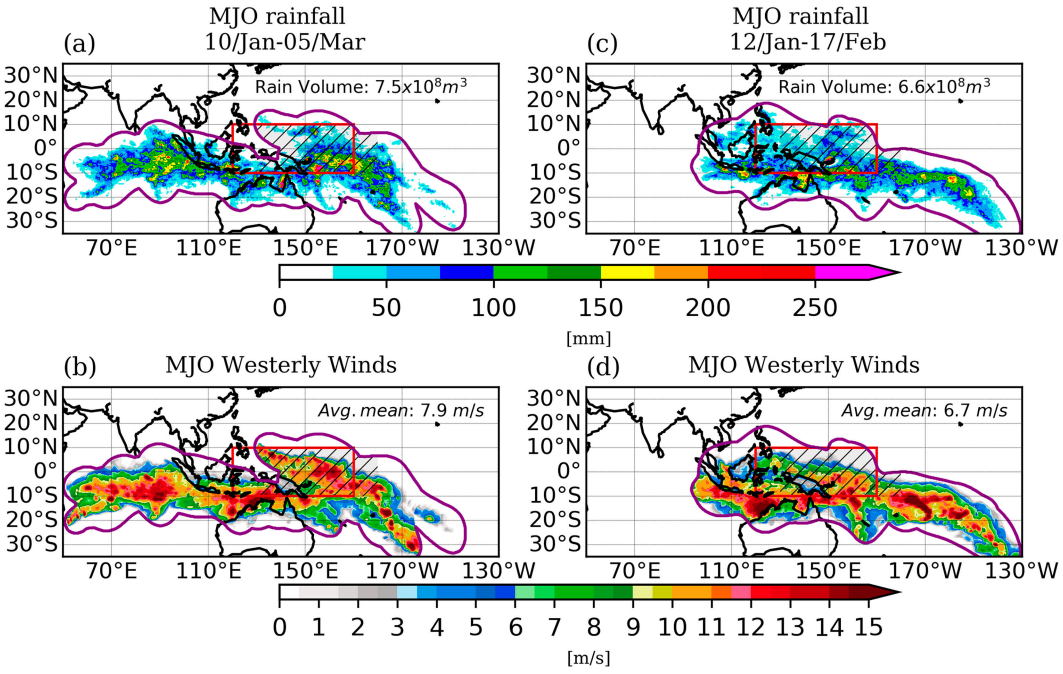

FIG. 2. MJO envelope (purple contour) indicates the area encompassed by the MJO-LPT feature for the two MJO events as shown in Fig. 1. (a),(c) Cumulative rainfall (mm) and (b),(d) average surface westerly wind speed (m s^{-1}) during the MJO LPTs. The red box marks the region of MJO impact on the warm pool (10°S–10°N, 130°E–180°). The total cumulative rain volume (m^3) and area-averaged wind speed (m s^{-1}) within the red box are given at the top right, respectively.

(e.g., Zhang 2005). The surface westerlies tend to be stronger than the easterlies due to the downward momentum transport within MCSs during the MJO's convectively active phase (Houze et al. 2000; Su et al. 2000; Mechem et al. 2002, 2006; Judt and Chen 2014). Observations have shown that convection, precipitation, and surface winds within the MJO's large-scale envelope exhibit multiscale variability, ranging from diurnal and bidiurnal to synoptic time scales (e.g., Chen et al. 1996; Chen and Houze 1997a). The characteristics of these variables can vary among different MJO events and can be directly modulated by ENSO on interannual time scales over the warm pool (e.g., Chen and Houze 1997b).

To assess the strength of the MJO and its direct influence on the SST and WPEE, we focus on two crucial measures: the total precipitation and surface westerly wind. They connect the ocean response directly to the MJO atmospheric forcing through the input of freshwater and momentum fluxes. In this study, the intensity of each MJO event is quantitatively defined by 1) the integrated rain volume from inside of each LPO through the entire MJO LPT (i.e., convectively active phase, in m^3) as described in Kerns and Chen (2020), and 2) 6-hourly maximum surface westerly winds (in m s^{-1}) inside each LPO and are averaged throughout the entire MJO LPT (Fig. 2). The MJO envelope indicates the area encompassed by the MJO feature smoothed with a 2.5° latitude–longitude Gaussian (purple contour in Fig. 2). The region 10°S–10°N, 130°E–180° represents the area of MJO impact on the warm pool shown in a red box. The MJO intensity of convection over the warm pool is defined as the rain integrated over the overlapping region between the MJO envelope and the red box. Similarly, the intensity of WWB is the average of westerlies during the MJO event over the same region in m s^{-1}. Thus, the intensity of each MJO event is quantified in terms of rain volume (m^3) and WWB (m s^{-1}).

To ensure that the results are representative of the warm pool, the analysis is repeated by varying the selected areas, for example by shifting and/or increasing longitude of 10° from 130°E to 180° in combination of changing latitudes from 10°S–10°N to 15°S–15°N. In general, the results are similar to that of 10°S–10°N, 130°E–180°.

d. *Post-MJO warm pool eastward extension*

The warm pool has traditionally been defined by various isotherms of the ocean surface, such as 28°, 28.5°, or 29°C in previous studies (Picaut and Delcroix 1995; Clarke et al. 2000; McPhaden and Picaut 1990; Picaut et al. 2001). This study defines the warm pool as the 28.5°C isotherm because it generally represents the large-scale warm pool feature over the tropical Pacific. The high-frequency SST variability was removed using a 3-day centered SST running mean and a two-dimensional Gaussian filter with a standard deviation of 10 grid points (2.5°, approximately 250 km near the equator). To accurately represent the warm pool evolution and the WPEE, we use the observed SST (not SST anomaly), which allows for direct tracking of the SST features in time (Graham and Barnett 1987; Jauregui and Takahashi 2018).

Brought to you by NOAA Central Library | Unauthenticated | Downloaded 08/13/24 07:09 PM UTC

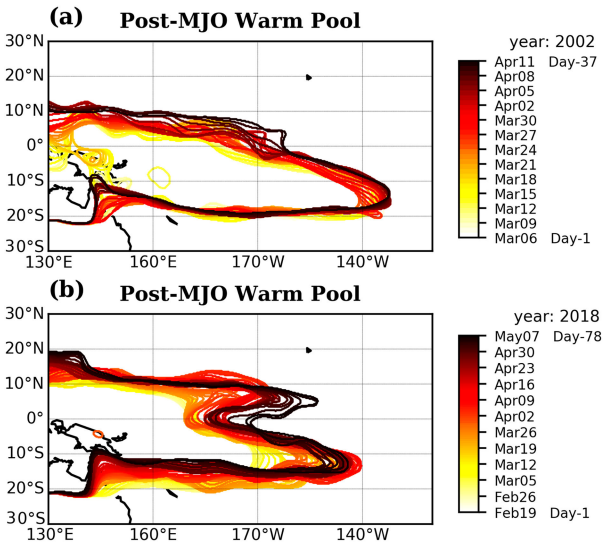

FIG. 3. Evolution of warm pool (28.5°C contour) after the two MJO LPT events shown in Fig. 1, from the post-MJO Day-1 onward: (a) March–April 2002 and (b) February–April 2018 with dates in color. Day-37 and Day-78 mark the day of the maximum WPEE (Day-max) for the two events, respectively.

Because the upper-ocean warming often occurs after the deep convection and precipitation associated with the MJO, as shown by Anderson et al. (1996), we track the eastern edge of the warm pool immediately after the end of the MJO LPT, which is defined as the beginning of the post-MJO precipitation phase as Day-0 (Fig. 1). Subsequently, we track the warm pool's movement from post-MJO Day-0 to Day-1, Day-2, and so on, as illustrated in Fig. 3. The warm pool is tracked only if its eastern edge moves eastward until reaching its maximum eastward displacement on Day-max. To determine the WPEE from Day-0 to Day-max, we calculate the warm pool displacement as the difference between the easternmost points of the warm pool on Day-0 and Day-max. We use the 0.25° data from 10°S to 10°N with a 5-day centered mean value of the equatorial band (5°S–5°N) to track the continuous WPEE in time, as shown in Figs. 4a and 4b. The maximum post-MJO WPEE and corresponding Day-max are marked in red for both cases in Figs. 4c and 4d. The tracking is terminated at Day-max if the equatorial warm pool retreats by more than 500 km or for more than 7 days.

This method provides a quantitative measure of the temporal and spatial WPEE during the post-MJO period. The maximum post-MJO WPEE associated with the two events is about 2500 km and occurred on Day-37 and Day-78, respectively (Figs. 3 and 4). To account for the 2.5° Gaussian smoothing applied to the SST fields, shorter displacements (<250 km) are classified as events with nondisplacement. Using this method, we identified 60 post-MJO WPEE events from the 98 MJO events (Table 1). Nine MJO events (IDs: 1, 3, 16, 27, 32, 40, 67, 80, 86) were associated with shorter post-MJO WPEE and classified as nondisplacement events. In some cases, the post-MJO warm pool displacement is westward; thus, we use the same criteria described above to identify the westward displacement.

e. WPEE anomaly

To further investigate whether the post-MJO WPEE is extended beyond the WP climatological position, we compute the WPEE anomaly. The WPEE anomaly is computed by subtracting its daily climatological longitude from 10°S to 10°N. The warm pool daily climatology retains the first three harmonics of the annual cycle from 1982 to 2010. Figure 5 shows the spatial variability of the monthly mean warm pool climatology. For example, the WPEE anomaly on Day-Max associated with the two MJO events from 2002 to 2018 is mostly positive, especially north of the equator, where the WPEE is about 3000 km farther east than their climatological positions (Figs. 6b,d). In contrast, a negative warm pool anomaly is observed south of the equator at about −1500 km for the 2018 MJO event (Fig. 6d).

3. Spatial structure and duration of the post-MJO WPEE

Using the LPT method to track the MJO events, as described in section 2b, made it possible to investigate the spatial and temporal structure and evolution of the MJO-induced SST changes during- and post-MJO events in this study for the first time. To illustrate how the new analysis tools are used for computing the post-MJO WPEE, we show two specific examples of the MJO events observed in 2002 (Fig. 7) and 2018 (Fig. 8).

The transition from La Niña in 2001 to El Niño in 2002 was proceeded by consecutive intense WWBs associated with the MJO events (McPhaden 2004). Figures 7 and 8 show multiple MJO events and WWBs prior to El Niño in May–June 2002 (Fig. 7d) and June–August 2018 (Fig. 8d). Warmer waters extending eastward to the Niño-3.4 region reduce the large-scale SST zonal gradient during El Niño, enabling favorable conditions for the development of the El Niño conditions in June 2022 and July 2018, respectively (Figs. 7c and 8c).

The evolution of the post-MJO WPEE SST changes during the transition from La Niña to El Niño, and surface winds from January–December 2002 are shown in Fig. 9. The MJO-induced SST anomalies develop over the tropical western Pacific (Fig. 9a) and extend toward central Pacific (Fig. 9b) with spatial scales that resemble the SST anomalies observed during the maturing phase of El Niño 2002 (Figs. 9d,e). The main difference is that the post-MJO WPEE occurs on shorter subseasonal time scales (i.e., weeks). As the multiple post-MJO WPEE events occur, the trade winds weaken significantly, as shown in Fig. 9, which are favorable for the development of El Niño. Similar features in SST and surface winds are observed during the onset of El Niño 2018 (not shown).

The observed MJO events during the onset of El Niño in 2002 and 2018 seemed favorable for developing El Niño. The questions that need to be addressed are (i) Is the post-MJO WPEE a common feature for all MJO events? (ii) How often do consecutive MJO events occur during the El Niño onset or prior to El Niño? and (iii) How are the magnitude and structure of the post-MJO WPEE affected by the MJO intensity of precipitation and surface westerlies? In the next three sections, we aim to address these questions using long-term satellite observations.

Brought to you by NOAA Central Library | Unauthenticated | Downloaded 08/13/24 07:09 PM UTC

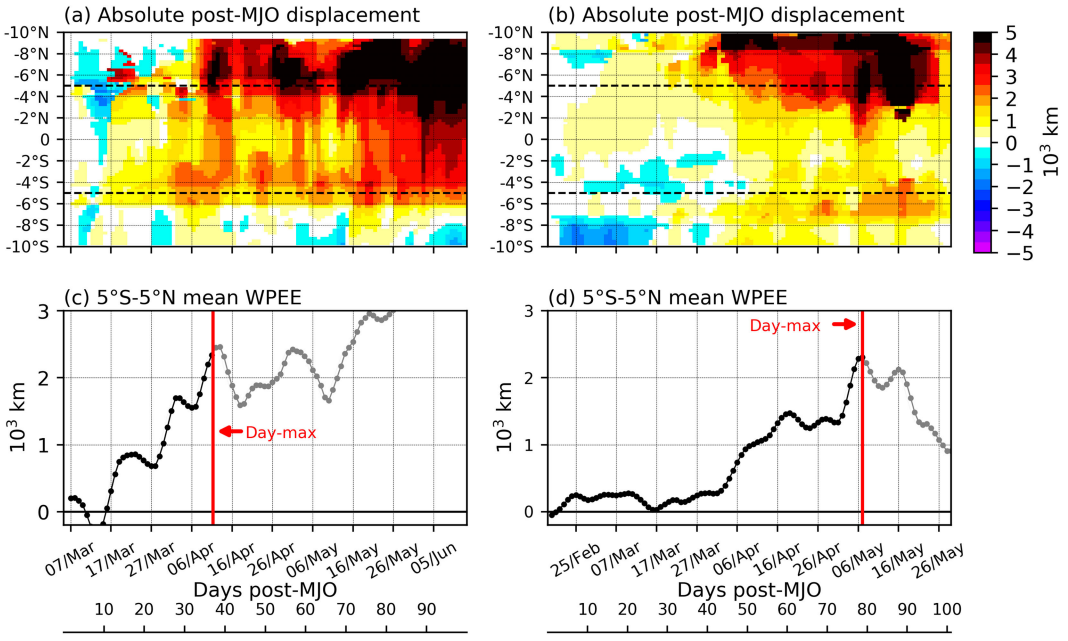

FIG. 4. (a),(b) Post-MJO warm pool displacement (10^3 km; colors) over time relative to positions on 5 Mar 2002 and 18 Feb 2018, respectively, from 10°S to 10°N. The black dashed lines enclose the equatorial band (5°S–5°N). (c),(d) Averaged warm pool displacement from 5°S to 5°N. The vertical red lines indicate post-MJO Day-max and the maximum post-MJO WPEE for the two MJO events, respectively, and the displacement shown in gray is discarded due to the 500-km retreat.

4. The MJO-induced WPEE in relation to ENSO from 1998 to 2019

The relationship between the post-MJO WPEE and ENSO is examined using observations from 1998 to 2019. Figure 10 shows the positions of the observed eastern edge of the warm pool and its climatology, warm pool anomaly, MJO events, absolute zonal surface wind speed, and the Niño-3.4 index representing ENSO conditions over the 21-yr period.

Tracking the post-MJO WPEE, as described in section 2c and quantified in section 2d, provides a better understanding of the relationship between MJO activity and the onset of El Niño events from 1998 to 2019. First, we identify periods of El Niño events according to the criteria developed by NOAA (2016). An El Niño advisory is issued when the Niño-3.4 index exceeds 0.5°C for five consecutive overlapping 3-month periods (https://origin.cpc.ncep.noaa.gov/products/analysis_monitoring/ensostuff/ONI_v5.php). The onset of each event was centered on June 2002, August 2004, September 2006, July 2009, October 2014, and October 2018 (red arrows in Fig. 10d).

Second, we examine the MJO events that could potentially contribute to the onset of El Niño. We focus on MJO events that occurred within 9 months before the onset of El Niño. This 9-month lag period is chosen based on the robust correlation observed by Kug et al. (2010) between precursors for the onset of El Niño (e.g., equatorial sea level, zonal mean thermocline) and the Niño-3.4 index. Using these criteria, we identified 25 MJO events within 9 months prior to El Niño events and 33 MJO events during El Niño events, marked in red and dark red in Fig. 10a, respectively. The remaining MJO events are not related to El Niño events (marked in black in Fig. 10a).

The enhanced MJO activity consistently precedes an anomalous WPEE before each observed El Niño event from 1998 to 2019 (Figs. 10a,b). During multiyear La Niña conditions in

TABLE 1. MJO events with identification numbers (ID) and their occurrences with an associated WPEE based on the ENSO state from 1998 to 2019.

	ENSO conditions		
	Non–El Niño	Within 9 months prior to El Niño	During El Niño
No. of events	23	20	17
MJO ID	2, 4, 5, 7, 8, 20, 31, 44, 45, 46, 48, 49, 50, 61, 62, 63, 66, 68, 70, 73, 74, 89, 91	9, 10, 11, 12, 24, 25, 34, 35, 36, 37, 38, 39, 51, 52, 75, 76, 77, 92, 93, 94	13, 14, 15, 17, 18, 26, 29, 42, 54, 55, 57, 59, 81, 85, 87, 97, 98

Brought to you by NOAA Central Library | Unauthenticated | Downloaded 08/13/24 07:09 PM UTC

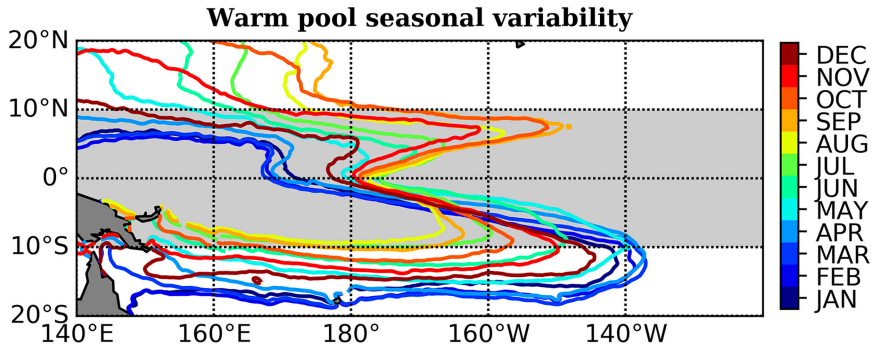

FIG. 5. Monthly climatology of the warm pool (28.5°C) from January–December (colors) computed using the OISST-V2 data from 1982 to 2010.

1999–2001 and 2010–12, the warm pool was positioned farther west. Although a detailed explanation of the differences in MJO activity and its impact on the warm pool displacement during La Niña conditions is beyond the scope of this study, Fig. 10 provides evidence that MJO events in early 2011 (61–63 in Fig. 10a) were followed by a WPEE of approximately 2000 km (Fig. 10b). This WPEE attenuated the equatorial negative Niño-3.4 anomalies and led to positive Niño-3.4 (Figs. 10c,d). Similarly, the MJO events from December 2016 to February 2017 were followed by a WPEE in May–June 2017, coinciding with relatively warm Niño-3.4 anomalies (Fig. 10a).

The 60 post-MJO WPEE events identified in section 2d are shown in Table 1. They are grouped relative to El Niño conditions. Among these 60 WPEE events, 20 occurred within 9 months preceding El Niño events, 17 occurred during El Niño events, and the remaining 23 occurred during neutral or La Niña conditions. Section 4a analyzes these results to characterize the spatial and temporal scales of these 60 WPEE events.

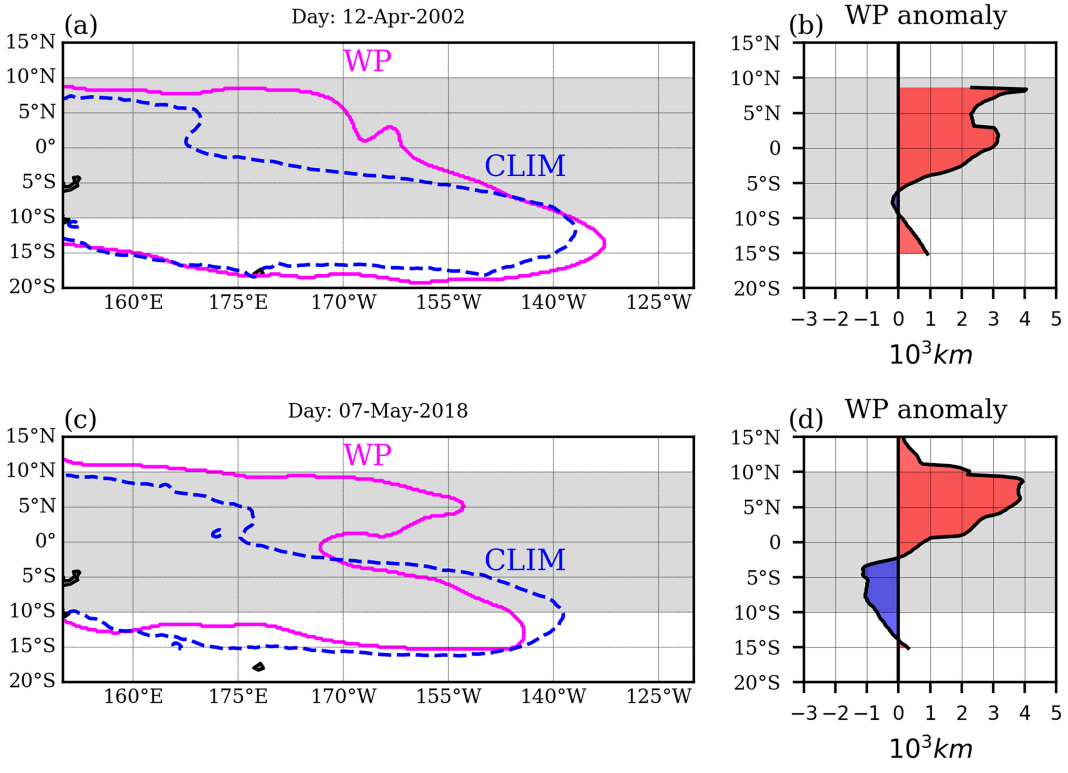

FIG. 6. (a),(c) Maximum eastward warm pool (28.5°C) location on 12 Apr 2002 and 7 May 2018, immediately after the two MJO LPT events as shown in Fig. 1 (magenta) and corresponding daily climatology (blue dashed lines). (b),(d) Anomalies computed as a difference of the warm pool absolute longitude relative to its climatology. Gray shading highlights the region between 10°S and 10°N.

Brought to you by NOAA Central Library | Unauthenticated | Downloaded 08/13/24 07:09 PM UTC

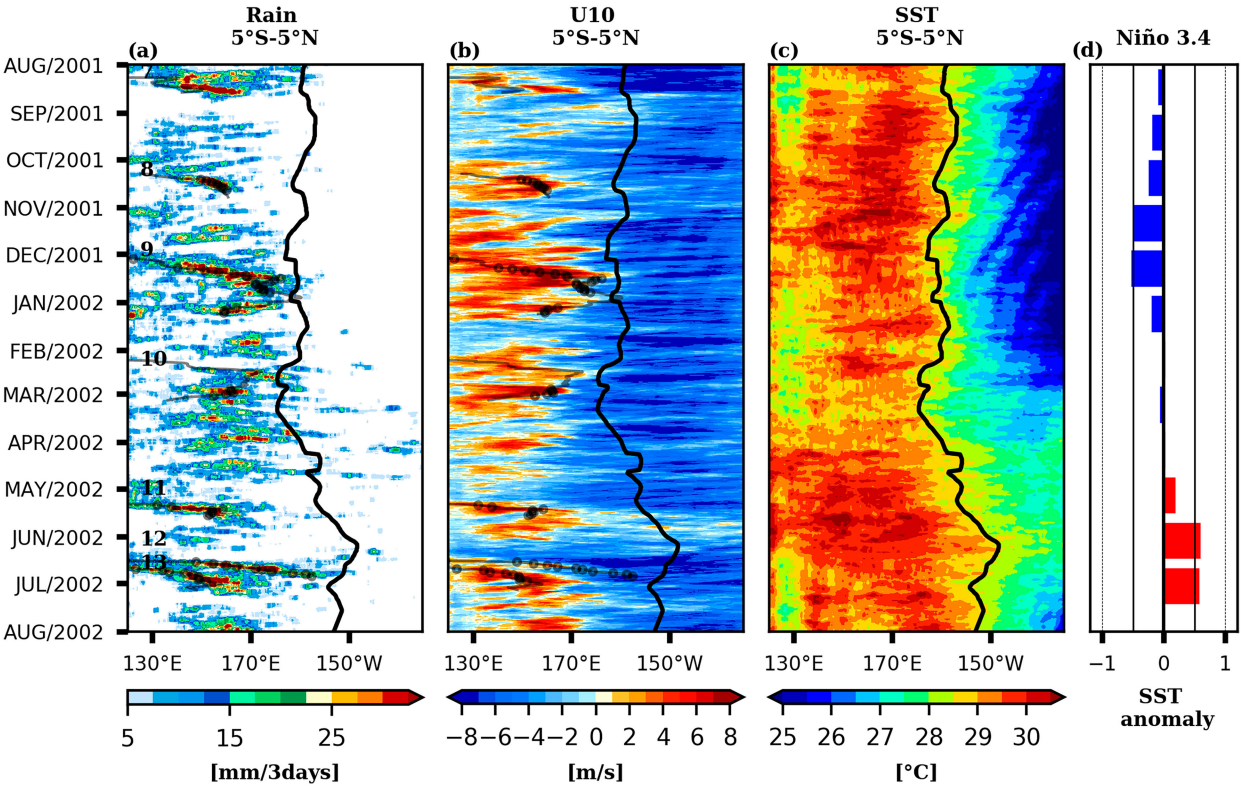

FIG. 7. Time–longitude sections of fields averaged over the equatorial zone of 5°S–5°N from August 2001 to August 2002 (a) 3-day accumulated rainfall, (b) 6-hourly surface zonal wind speed, (c) daily SST, and (d) Niño-3.4 monthly anomalies. The position of equatorial warm pool is shown in black contours in (a)–(c). The MJO LPT centroids for the MJO events 7–13 (Table 1) are shown in (a) and (b).

a. MJO-induced WPEE

We examine the displacement of the eastern edge of the warm pool over the equatorial band (5°S–5°N) before and after the MJO ending date (Day-0) for the 60 events identified in sections 2c and 2d. Instead of using the average, we analyze individual grid points within the equatorial band because the warm pool does not move monotonically, as shown in Figs. 4a and 4b. In Fig. 11a, we present the frequency of zonal displacement over the equatorial band. In agreement with Drushka et al. (2015), the warm pool displacement is slightly more westward than eastward, during the MJO active phase. However, eastward displacements are much more common, pronounced, and long lasting (represented by red bars in Fig. 11a) during the post-MJO period, especially during the first 15–20 days, with displacements beyond 1000 km. The net impact of the MJO including both the convectively active and suppressed phases on the warm pool is predominantly eastward displacements (i.e., positive WPEE) (Fig. 11a).

The joint histogram of displacement of all grid points within the equatorial band of 5°S–5°N shown in Fig. 11b is computed as a function of days relative to Day-0. The most frequent WPEE occurs during the first 15 days with displacements up to 1000 km (Fig. 11b). These spatial and temporal scales give a WPEE speed of about 0.8 m s^{-1}, close to the eastward Yoshida jet speed of 1 m s^{-1} (Yoshida 1959; Ralph et al. 1997) but slower than ocean Kelvin waves (2 m s^{-1}). If an MJO-westerly event occurs at 150°E and the warm pool eastern edge is located between 170°E and 175°W, the time it takes for the oceanic Kelvin wave to reach the warm pool edge is about 12–22 days. On average, the WPEE duration and displacement after MJO events are within the range of an oceanic Kelvin wave propagation. However, other processes at these short time scales are also at work (e.g., nonlinear advection terms, strong zonal salinity gradient in driving surface currents jets, air–sea fluxes).

We found that 60 out of the 98 MJO events (61%) from 1998 to 2019 produced WPEE (Fig. 11). Among the 60 events, most of them (71%) induce a WPEE during the first 15 days, and 53% sustain a WPEE beyond 20 days. It is noteworthy that sustained and progressive post-MJO WPEE do not occur during El Niño periods. This is because, during the developing phase of El Niño, the warm pool is already located over the central-eastern Pacific and remains stationary.

b. MJO-induced WPEE in relation to El Niño

Here we examine the MJO position in the western Pacific in relation to the WPEE, based on the three groups shown in Table 1. To better understand the meridional extent of the WPEE, we expand the analysis from 5°S–5°N to 10°S–10°N. The MJO with a larger zonal extent is expected to induce a

Brought to you by NOAA Central Library | Unauthenticated | Downloaded 08/13/24 07:09 PM UTC

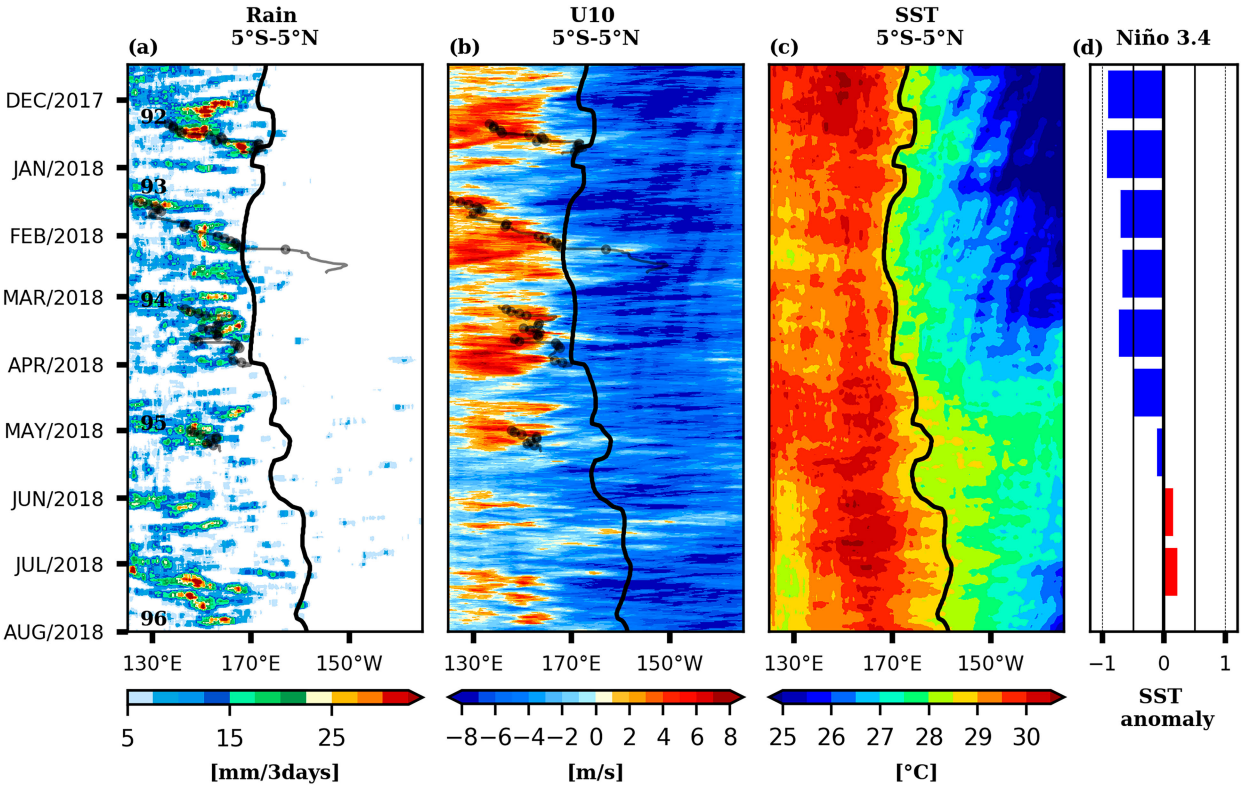

FIG. 8. As in Fig. 7, but for November 2017–August 2018.

larger WPEE. Conversely, the MJO propagating off-equatorial may have a less direct impact on the WPEE. To test this hypothesis, we compare the extent of MJO propagation and the associated WPEE within each group as defined in Table 1.

We analyze the initial and ending longitude locations of the MJO tracks for each event within each group (Figs. 12a–c). These tracks provide an indication of the zonal extent of MJO propagation. Additionally, we compute the anomalous displacement by taking the difference between the warm pool anomaly at Day-Max and Day-0 from 10°S to 10°N. The composite analysis, along with the 95% confidence intervals for each group (Figs. 12d–f), demonstrates that the anomalous WPEE is a robust signal.

The group of events prior to El Niño (Fig. 12e) induced larger anomalous WPEE (up to 2000 km), especially in the equatorial region but with a more pronounced effect in the Northern Hemisphere. These events started with an anomalous warm pool position of about 500 km at 5°N, which indicates that the WPEE began during the MJO event, consistent with Fig. 11a. In the case of the El Niño group, the warm pool was already in an unusually eastern position (not shown), and further eastward expansion could be attributed to both the MJO events and El Niño development (Fig. 12f). The events unrelated to El Niño showed relatively shorter displacements, up to 1000 km (Fig. 12d). The impact of the MJO on the warm pool is more evident along the equatorial band (5°S–5°N) and in the northern tropical hemisphere (5°–10°N) for the events occurring before and during El Niño (Figs. 12e,f).

c. *Composite of MJO-induced WPEE prior to El Niño*

The overall effects of warm pool displacement on SST anomalies associated with MJO events prior to El Niño are shown in Fig. 13. We found that MJO-induced WPEE before El Niño occurred under slightly warmer anomalies between 160° and 175°E (Fig. 13a). The most substantial warming occurs during the post-MJO period (Fig. 13b). The difference between the post-MJO and during-MJO SST anomalies is shown in Fig. 13c. It is important to note that the net post-MJO SST anomaly is much stronger and farther east than during the MJO, which is consistent with the MJO-induced WPEE shown in Fig. 11a. This MJO-induced positive SST anomaly is observed mostly along the equator and specifically associated with MJO events prior to El Niño (Fig. 13c). While the maximum warming is over the central Pacific (175°E–170°W), a significant portion of this MJO-induced SST warming before El Niño is concentrated within the Niño-3.4 region (east of 170°W), with SST anomalies exceeding 0.5°C. This finding suggests that MJO events directly contribute to the SST increase in the Niño-3.4 region and, consequently, the onset of El Niño.

The post-MJO-induced warming shown in Fig. 13b will be favorable for the occurrence of subsequent MJO events in the western-central Pacific. These consecutive MJO events are often associated with a progressive eastward displacement of the warm pool, particularly during boreal winter, and will be discussed in the following section.

Brought to you by NOAA Central Library | Unauthenticated | Downloaded 08/13/24 07:09 PM UTC

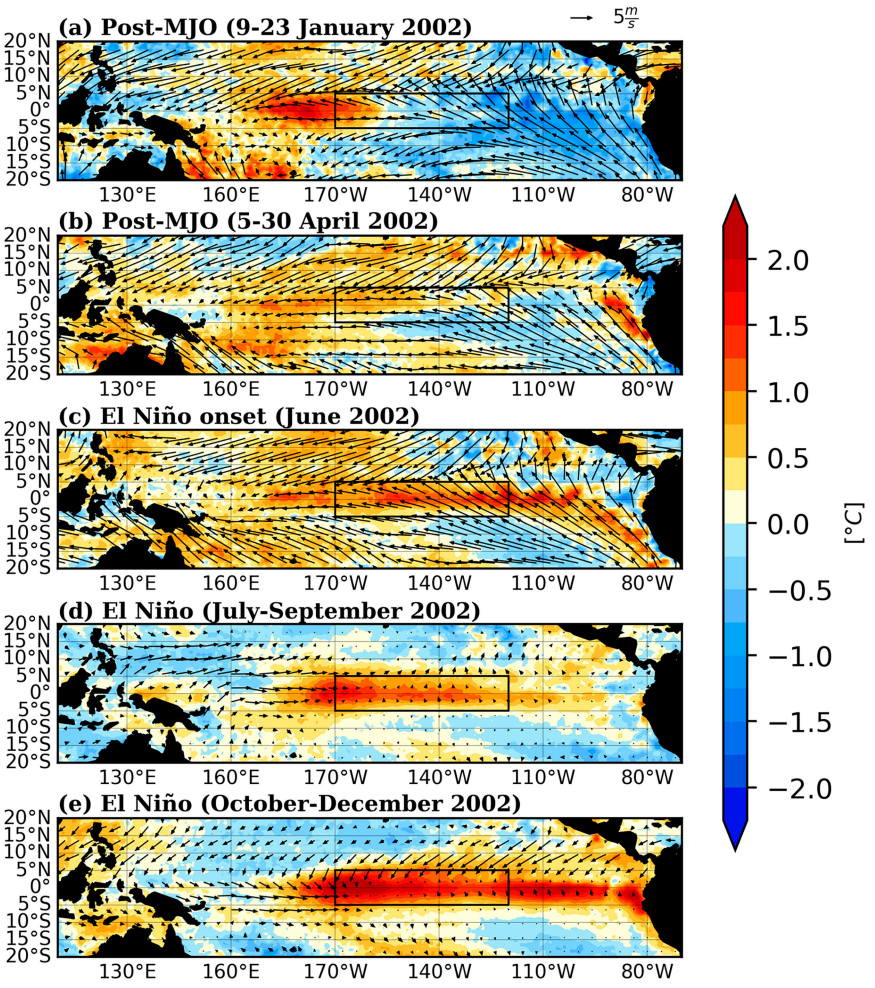

FIG. 9. Surface wind anomalies (vectors) and SST anomaly (colors; °C) for two post-MJO periods (a) from 9 to 23 Jan 2002 associated with the MJO (11, Table 1) and (b) 5–30 Apr 2002 (12, Table 1), (c) El Niño onset in June 2002, maturing stages in (d) July–September and (e) October–December 2002. The black box in all panels corresponds to the Niño-3.4 region.

5. Seasonal variability of the MJO and WPEE

a. Annual cycles of the MJO and MJO-induced WPEE

The MJO events and their impacts on WPEE have a pronounced seasonal cycle. The 60 MJO events that produced a WPEE (Table 1) are more frequently observed in the western Pacific during boreal winter and early spring, shifting toward the South Pacific convergence zone (SPCZ) (Fig. 14a). Conversely, weak MJO activity occurs in summer and fall, with centers of MJO precipitation shifting toward the Northern Hemisphere during the active Asian monsoon. The equatorial warm pool has a significant annual cycle, migrating from 170°E to 170°W from boreal spring to summer (dashed blue lines in Fig. 14). However, during neutral ENSO conditions, the post-MJO equatorial warm pool displacement extends far beyond the climatological position, especially from February to June (orange lines in Fig. 14b).

MJO events with a significant impact on the WPEE are often observed during boreal spring, and these events can sustain displacements exceeding 2000 km (Fig. 15). MJO events occurring from January to April are more likely to reach the warm pool's eastern edge (Fig. 14a) and induce an eastward expansion (Fig. 14b). On the other hand, MJO events from June to August have a less direct impact on the warm pool eastern edge unless they propagate farther east toward the vicinity of the warm pool eastern edge. The Southern Hemisphere warm pool's eastern edge is less directly affected by MJO events due to its far-east location (Fig. 5), unless MJO events propagate south into the SPCZ, which occurs during boreal winter (Figs. 14 and 15).

By examining the number of MJO-induced WPEE by month (Fig. 15), we confirm that there are more MJO events in boreal winter and spring compared to the rest of the year. The boreal spring (March–May) has the most MJO events

Brought to you by NOAA Central Library | Unauthenticated | Downloaded 08/13/24 07:09 PM UTC

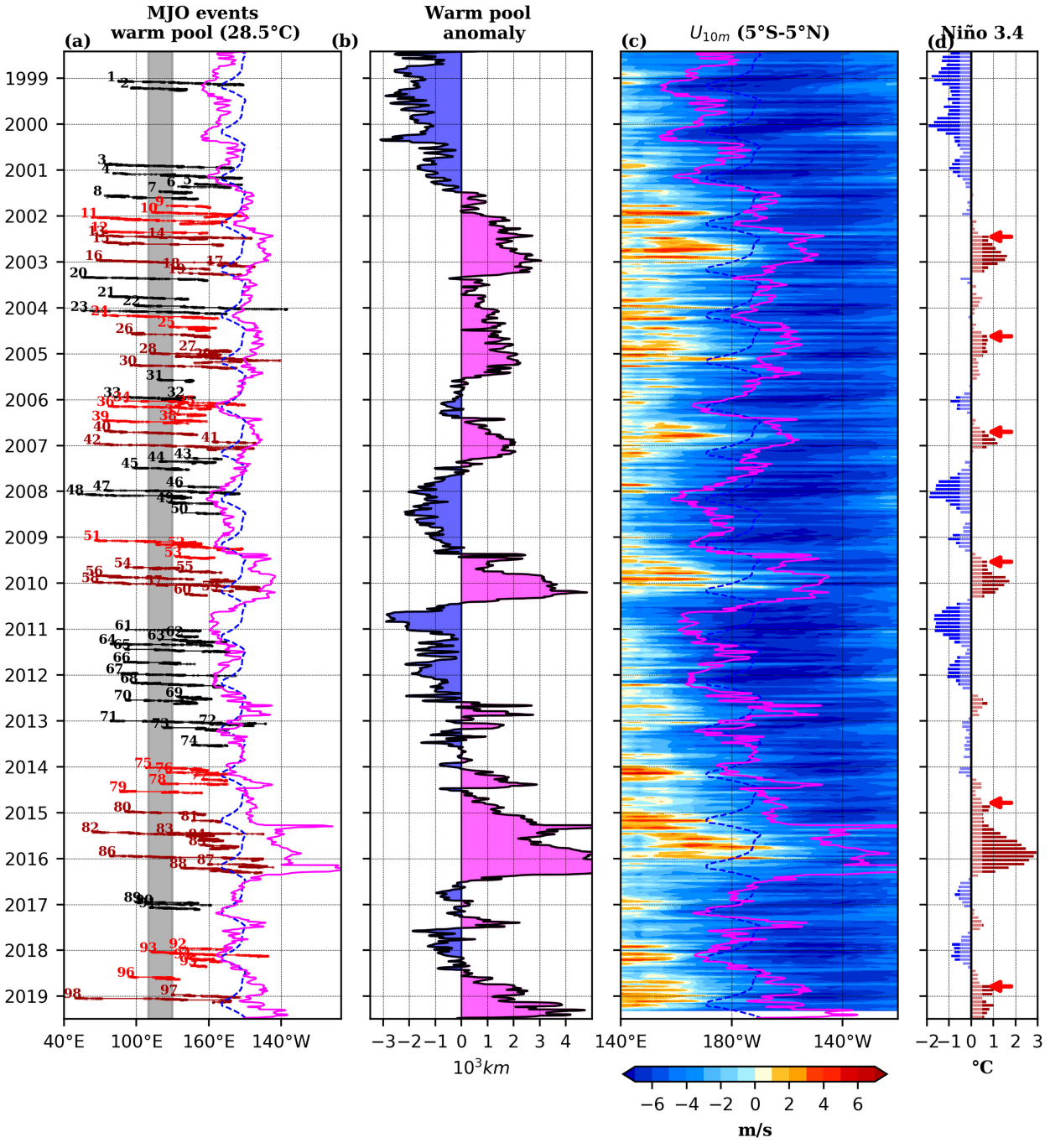

FIG. 10. (a) Eastern edge of equatorial warm pool (28.5°C; magenta) averaged from 5°S to 5°N and its climatological position (blue dashed) from 1998 to 2019. The MJO events occurring within 9 months prior to the El Niño onset are shown in red, during El Niño in dark red, and the remaining events in black. The Maritime Continent (110°–130°E) is marked in gray. (b) The WPEE negative and positive anomalies (10^3 km) shaded as blue and magenta, respectively. (c) Equatorial surface zonal winds from CCMP. (d) Niño-3.4 SST anomaly (3-monthly averages) > 0.5°C (<−0.5°C) shown in red (blue). Red arrows indicate the onset of each El Niño event.

and the largest WPEE in both non-El Niño (Figs. 15a,c) and onset of El Niño (Figs. 15b,d) conditions. These findings are consistent with previous studies (Moore and Kleeman 1999; Hendon et al. 2007) that have identified boreal spring as the time when the growth of ENSO SST anomalies is most sensitive to MJO forcing. This means that if MJO activity is elevated during spring, the WPEE leads to strong basinwide warm SST anomalies in the equatorial Pacific (McPhaden et al. 2006b), leading to the development of El Niño the following boreal winter as was demonstrated with robust lagged

Brought to you by NOAA Central Library | Unauthenticated | Downloaded 08/13/24 07:09 PM UTC

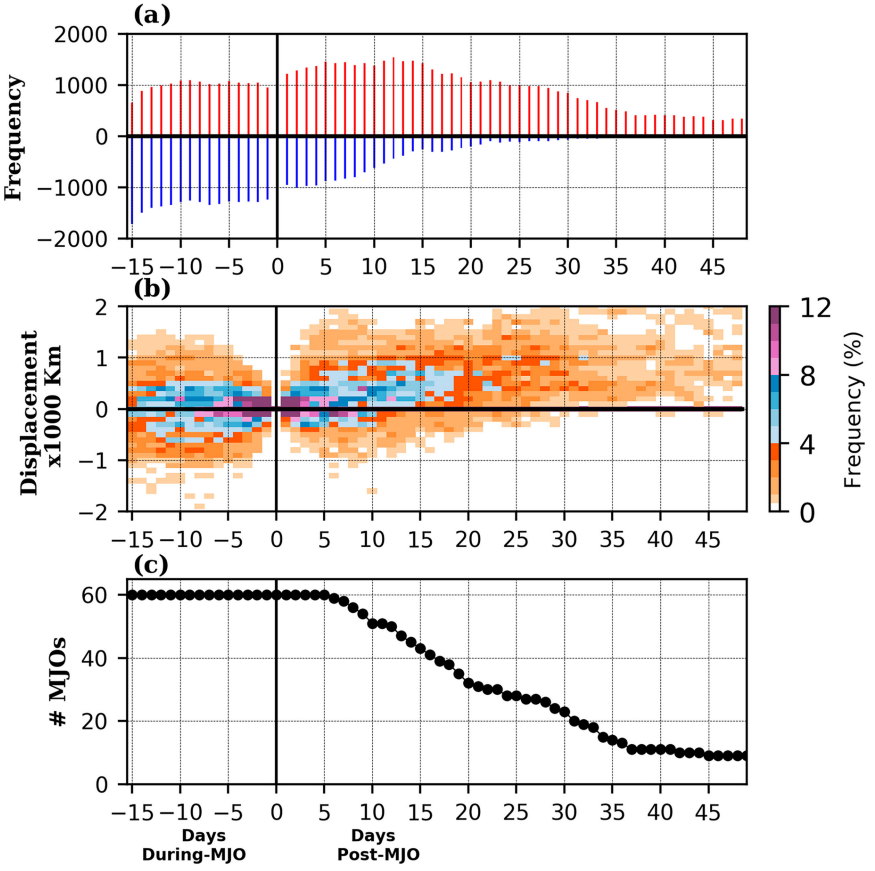

FIG. 11. Equatorial (5°S–5°N) warm pool eastern edge displacement as a function of days during and post-MJO precipitation from 1998 to 2019. (a) Frequency of displacement (number of the equatorial band grids per day), red color indicates eastward displacement, and blue colors indicate westward displacement. (b) Joint histogram of the warm pool eastern edge displacement (10^3 km) and frequency. (c) Number of MJO events as a function of days during- and post-MJO precipitation.

correlations between MJO-filtered equatorial variables (OLR and zonal surface wind speed) and Niño-3.4 SST index by Hendon et al. (2007).

6. Effects of the MJO intensity on WPEE

To further quantify the MJO's impacts on the warm pool displacement in relation to El Niño onset, we examine how the MJO intensity, as defined in section 2c, affects the warm pool displacement prior to El Niño. This analysis excludes the 33 MJO events that occurred during El Niño from 1998 to 2019. Among the remaining 65 events observed in non–El Niño conditions, 43 produced a positive WPEE (see Table 1) and 22 negative or zero WPEE. Figure 16 shows the WPEE in relation to the MJO intensity as defined by the total rain volume (Fig. 16a) and WWB (Fig. 16b). The MJO events that occurred prior to El Niño are shown by red squares, whereas events that are unrelated to El Niño are shown by gray circles. The MJO intensity in terms of rain volume varies from 0.3 to 16×10^8 m^3 with a mean of 4.6×10^8 m^3, and WWBs from 3 to 9 m s^{-1} with a mean of 5.7 m s^{-1} (Fig. 16c).

Most MJO events occurred prior to El Niño produced positive WPEE, whereas more non–El Niño events are negative WPEE than positive (Figs. 16a,b). The strongest MJO events (largest rain volume and highest WWB) precede El Niño (Fig. 16c). However, few intense MJO events are associated with warm pool westward displacement because these events occurred during unfavorable background conditions. For instance, during June 2014 (e.g., MJO 78–79 in Fig. 10), very strong trade (easterly) winds can counteract the WPEE and cause the initial eastward displacement to retreat. Each MJO event differs in terms of duration, structure, and intensity (Fig. 1), and the MJO-induced WPEE depends on its relative position to the warm pool eastern edge, as well as the oceanic and atmospheric conditions (e.g., Bergman et al. 2001; Fedorov et al. 2015; Puy et al. 2016).

Consecutive MJO events can collectively affect the ocean state on longer time scales (e.g., Kessler and Kleeman 2000; Bergman et al. 2001). We found that six consecutive cases occurred prior to El Niño (9–12, 24–25, 34–39, 51–52, 75–77, and 92–94), two during El Niño conditions (54–55, 26–27), and five cases during cold or neutral conditions (3–5, 7–8, 43–45, 48–50, 61–63) as shown in Fig. 10.

Brought to you by NOAA Central Library | Unauthenticated | Downloaded 08/13/24 07:09 PM UTC

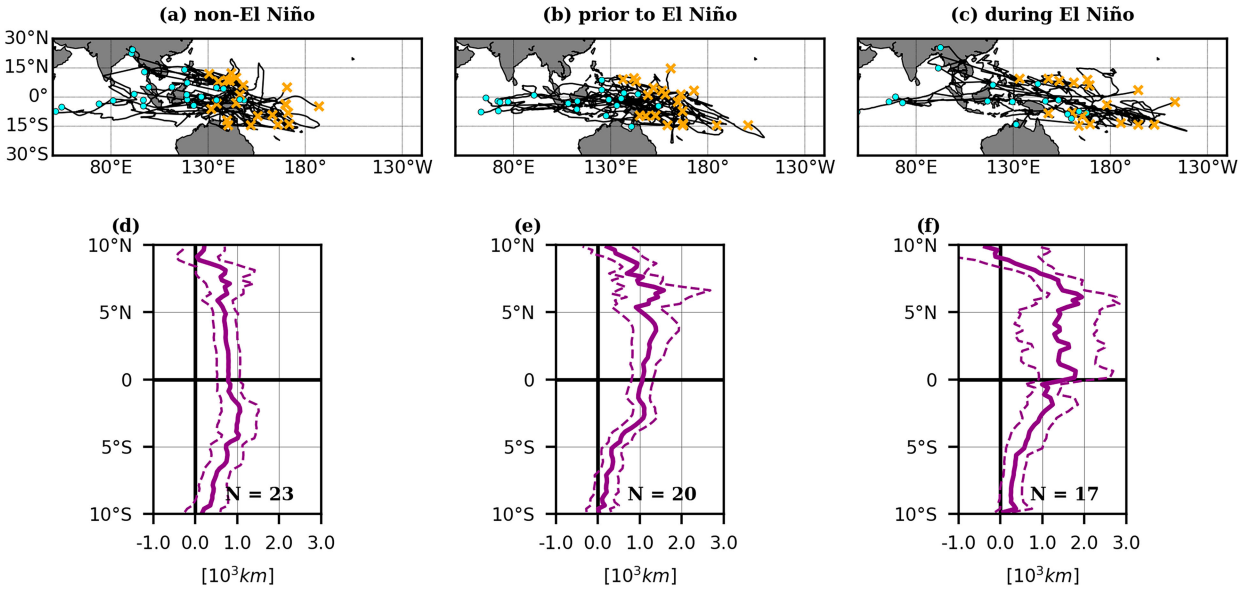

FIG. 12. Tracks of the MJO centroid of the MJO events for (a) non-El Niño related, (b) prior to El Niño, and (c) during El Niño. Cyan dots and orange crosses mark the start and end of the tracks. (d)–(f) The WPEE composite as a function of latitude, every 0.25°, computed as the difference of the warm pool anomaly at Day-max and Day-0. Dashed lines show the confidence intervals ($\alpha = 0.05$). The number of the MJO events per group are shown in (d)–(f).

Figure 16d highlights the difference between the consecutive MJO events that occurred prior to El Niño (squares) and the remaining consecutive MJO events (circles) shown as in accumulated rain volume of individual events, and the WWB corresponds to the maximum within the group. The total WPEE of consecutive events is shown in color, and the sizes of squares are proportional to the number of events. As expected, larger WPEE is associated with consecutive MJO events by strong WWBs and large accumulated rain volume, especially before El Niño. Each El Niño event is preceded by 2–6 MJO events associated with significant WPEE ranging from 1500 to 4000 km. These results support the premise that the MJO group effort has a more significant impact on the WPEE.

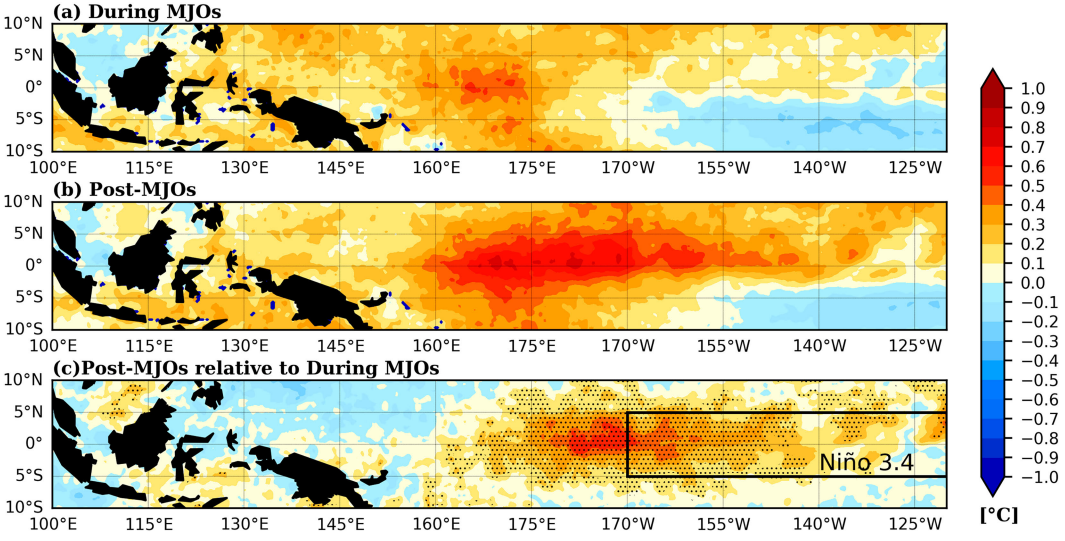

FIG. 13. Composite of SST anomaly for the MJO events prior to El Niño (a) during the MJO LPTs (convectively active phase), (b) in the post-MJO LPT period from Day-1 to Day-max, and (c) the difference between the post-MJO and the MJO SST anomaly. The black box indicates the Niño-3.4 region and stippling marks locations with significantly warmer at 95% confidence level.

Brought to you by NOAA Central Library | Unauthenticated | Downloaded 08/13/24 07:09 PM UTC

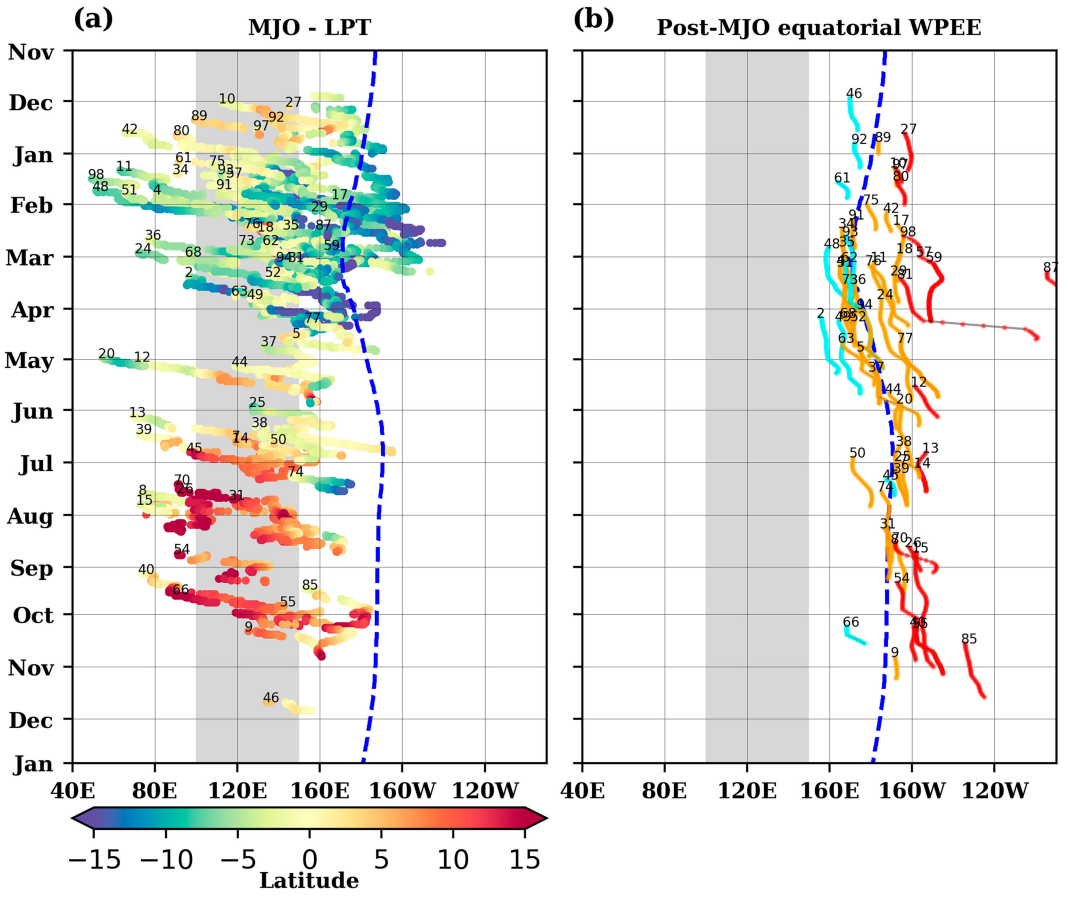

FIG. 14. (a) Annual cycle of the MJO events from 1998 to 2019 that produced a post-MJO WPEE varying with longitude and latitude (colors). Numbers indicate the MJO identification number. (b) The corresponding post-MJO equatorial WPEE colored by the Niño-3.4 state. Cyan, orange, and red colors correspond to cold, neutral, and warm ENSO states, respectively. The dashed blue contour marks the climatology of the eastern edge of the equatorial warm pool. Gray shading indicates the Maritime Continent region.

The large WPEE associated with consecutive MJO events results from the long-term effect of MJO forcing on the upper ocean and is commonly observed as large-scale SST anomalies in the equatorial Pacific Ocean. Consequently, these warm anomalies can weaken the trade winds (Fig. 10c). Under favorable atmosphere and ocean conditions this initial warming can further grow associated with positive coupled atmosphere–ocean processes allowing the warm pool to shift farther east during El Niño development. Consecutive MJO events unrelated to El Niño (Fig. 16d) also exhibit relatively strong convection and westerlies; however, they induce a relatively short WPEE and are not followed by El Niño.

To compare the consecutive MJO events prior to and non–El Niño, we composite the accumulated rainfall volume and the averaged WWB within the MJO LPT feature from 5°S to 5°N (Fig. 17) for both groups. We then compute confidence intervals at the 95% level, shown in gray and red shading, respectively, in Fig. 17. Composites of rain volume and WWB during the MJO propagation gradually increases from 30° to 160°E in both groups. However, events prior to El Niño are significantly stronger at 95% than the non–El Niño–related events, particularly east to 150°E. These results indicate that MJO events preceding El Niño propagate farther eastward than the other events. The net local impact of the MJO prior to El Niño spans from 150°E to 170°W, and increases SST anomalies to the east into the Niño-3.4 region, as observed in Fig. 13c.

7. Summary and conclusions

This study examines the MJO-induced WPEE using 21 years of satellite observations of precipitation, surface winds, and SST data from 1998 to 2019. We use the MJO LPT method developed by Kerns and Chen (2016, 2020) to identify the actual MJO precipitation and track it in time and space. This method allows us to directly examine the impacts of the MJO precipitation and westerly winds on the extension of the warm pool during both convectively active and suppressed phases of the MJO. For the first time, we can quantitatively analyze the temporal and spatial characteristics of all MJO-induced WPEE, including those occurring prior to El Niño events (Figs. 3, 11, and 15).

Brought to you by NOAA Central Library | Unauthenticated | Downloaded 08/13/24 07:09 PM UTC

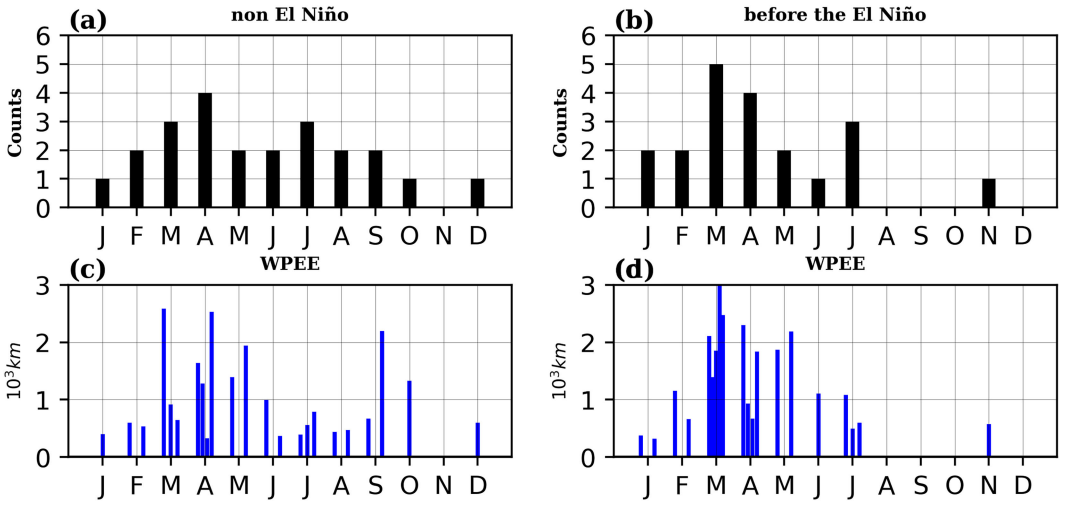

FIG. 15. Seasonal variability of the MJO events by month from January to December: (a) non–El Niño related and (b) prior to El Niño onset from 1998 to 2019. (c),(d) The Max-WPEE (blue; km) associated with each MJO event shown in (a) and (b).

Our analysis shows that the majority of MJO events (61%) in the equatorial western-central Pacific region induce a WPEE ranging from 1000 to 3000 km for 15 days after the MJO LPTs (convectively active phase). Additionally, about 20% of MJO events lead to a continuous and long-lasting WPEE exceeding 3000 km for more than 20 days. The timing and spatial characteristics of post-MJO WPEE provide valuable insights for understanding and predicting subsequent MJO precipitation, WWBs, and the overall impacts of the MJO.

The net impact of the MJO including both the convectively active and suppressed (post-MJO) phases on the warm pool is predominantly eastward displacements (positive WPEE; Fig. 11a). The post-MJO SST anomaly is much stronger and farther east than during the MJO convectively active phases, which is consistent with the MJO-induced WPEE shown in Fig. 11a. This MJO-induced positive SST anomaly is observed mostly along the equator and specifically associated with MJO events prior to El Niño (Fig. 13c)

It is worth noting that MJO events prior to El Niño are significantly stronger as measured by substantial rain volume and intense WWBs (Figs. 16 and 17). These events can induce a substantial WPEE exceeding 2000 km (Figs. 16a,b), which is robust and extends beyond the typical annual cycle (Figs. 12–14). These MJO events have a pronounced intensity of rainfall and WWBs along the equator (5°S–5°N) between 150° and 170°E, west of the Niño-3.4 region (Fig. 17). More importantly, they contribute to a large-scale warm SST anomaly exceeding 0.5°C in the Niño-3.4 region, which is significant for El Niño development (Fig. 13).

The MJO-induced WPEE is particularly large prior to each El Niño in all six events over 21 years from 1998 to 2019 (Fig. 16d). The intensity of rain volume and WWBs of the grouped consecutive MJO LPTs is directly related to the WPEE distance. The impacts of consecutive MJO events on the ocean have long-term atmospheric and oceanic implications, often manifesting as changes in trade wind intensity and subsurface temperatures across the equatorial Pacific basin, as observed prior to the onset of El Niño events in 2002/03 and 2018/19 (Figs. 7–9).

There is a distinct seasonal variability in the MJO-induced WPEE. During boreal winter and early spring (Fig. 14), the MJO's track density reaches the date line's vicinity (Fig. 12). Significant MJO-induced WPEE anomalies (>1000 km) occur during the transition from boreal spring to summer (Figs. 14c,d), which coincides with the warm pool's seasonal migration (Fig. 5). These results confirm the role of MJO forcing on the western Pacific during boreal spring when the zonal SST gradient is weak, and the atmosphere–ocean coupled system is relatively unstable to SST changes (Latif et al. 1994).

Several key conclusions can be drawn from the results presented in this study:

1) 61% of the 98 MJO events induced a WPEE over 1000–3000 km along the equator over the western-central Pacific, which can last beyond 15–30 days after the MJO precipitation,
2) The MJO events that occurred prior to El Niño onset are generally stronger (i.e., greater total volume of rain and stronger surface westerly winds) and produce significant WPEE far beyond its annual cycle (up to 1000 km), which can contribute to positive SST anomaly in the Niño-3.4 region,
3) Consecutive MJO events can produce much stronger WPEE prior to El Niño onset, which are observed in all El Niño events from 1998 to 2019, and
4) More frequent MJO events and stronger MJO-induced WPEE occur in March–May than in other seasons.

These results can help better understand the MJO–ENSO interaction and improve the prediction of the onset of El Niño. We provide quantitative analysis based on observations, which are consistent with previous studies on the MJO in connection to El Niño onset (e.g., Kessler et al. 1995;

Brought to you by NOAA Central Library | Unauthenticated | Downloaded 08/13/24 07:09 PM UTC

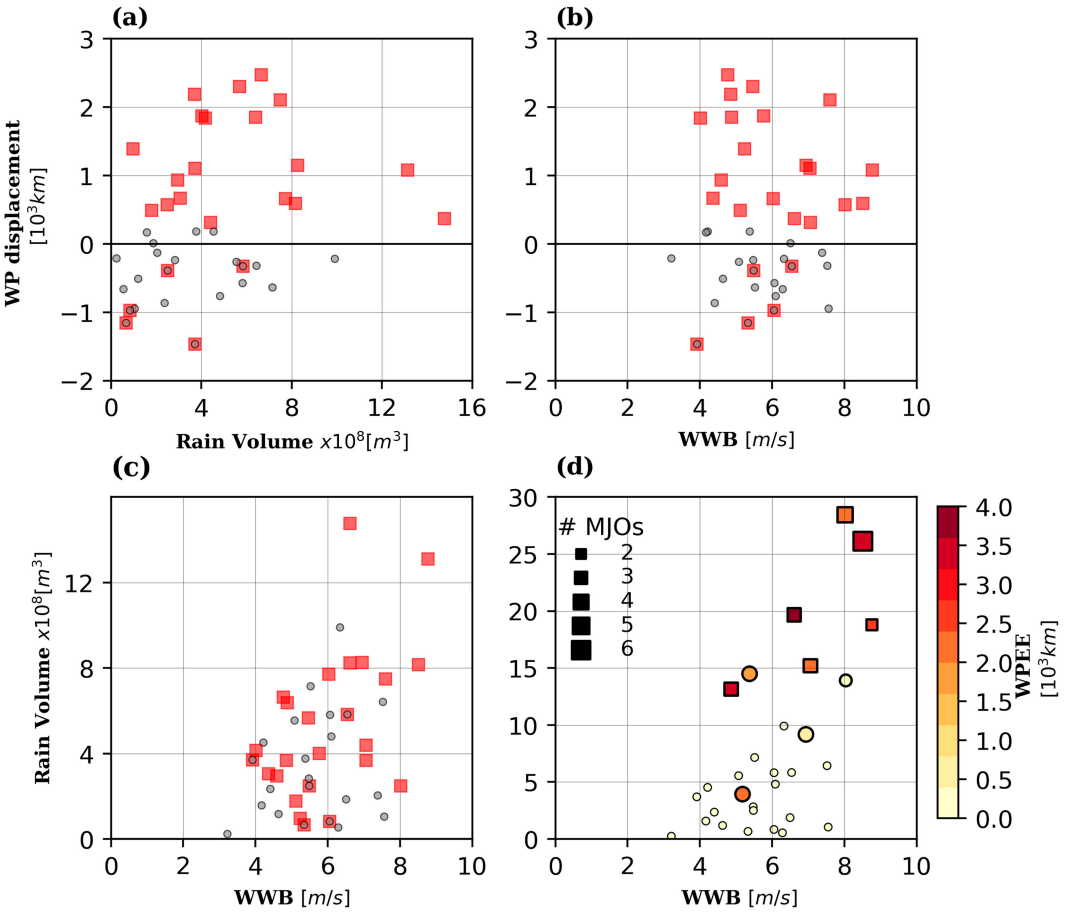

FIG. 16. Post-MJO warm pool displacement as a function of (a) total rain volume (m^3) and (b) westerly wind burst (WWB; averaged wind speed; m s^{-1}). The MJO events occurred prior to the El Niño are shown in red squares and non–El Niño related in gray circles. (c) Post-MJO WPEE (km) in relation to the total rain volume and WWB. (d) The MJO events prior to each El Niño are grouped together and their cumulative WPEE are shown in colored squares. The non–El Niño related consecutive events are grouped and shown in colored circles. The size of the squares is proportional to the number of the MJO events in each group. Note that the MJO events occurred during El Niño are excluded in all panels.

Shinoda and Hendon 2001; Zhang and Gottschalck 2002; Hendon et al. 2007).

One implication of the MJO-induced WPEE and its contribution to the onset of El Niño is that coupled atmosphere–ocean processes may interact from intraseasonal to interdecadal time scales, as demonstrated by Kerns and Chen (2021). Improving coupled Earth system models could be a key to better modeling and predicting the MJO (e.g., Savarin and Chen 2022a,b) and ENSO, especially for forecasts of the onset of El Niño that start in boreal spring (Barnston et al. 2012; Zhao et al. 2016). A good representation of the MJO precipitation and surface winds over the warm pool at longer time scales may reduce the model bias in the CMIP5 models (Brown et al. 2014). The physical mechanism(s) responsible for the MJO-induced upper-ocean warming and its eastward extension are not yet fully understood. Studies using a high-resolution coupled atmosphere–ocean model based on the recent study by Kerns and Chen (2021) and global coupled model reanalysis with observations from 1979 to 2023 on the MJO influences on the eastward extension of the warm pool leading to El Niño onset are underway. Furthermore, the Tropical Pacific Observing System (TPOS) program can provide observations that are urgently needed to shed new light on this important problem in the future.

Acknowledgments. We thank Brandon Kerns and Ajda Savarin for their assistance on the MJO LPT analysis, and Chidong Zhang for helpful discussions on the MJO and ENSO interaction. This research is supported by the NOAA CVP Grants NA15OAR4320063 and NA18OAR4310401. The first author is partially supported by the National Fund for Scientific, Technological Development and Technological Innovation (FONDECYT), the funding branch of the National Council for Science, Technology and Technological Innovation (CONCYTEC) Peru (094-2016-FONDECYT) and a NASA

Brought to you by NOAA Central Library | Unauthenticated | Downloaded 08/13/24 07:09 PM UTC

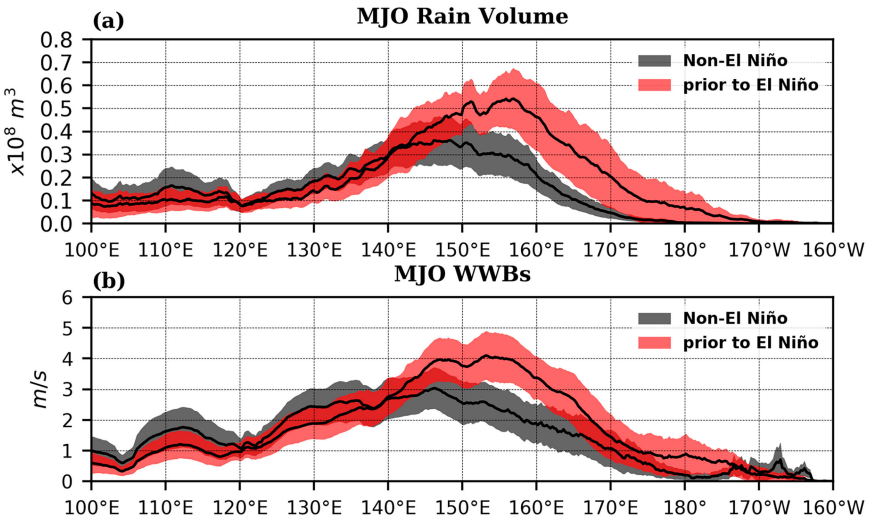

FIG. 17. (a) Total rain volume (m^3) and (b) averaged WWB wind speed (m s^{-1}) during the MJO LPTs (convectively active phase) from 5°S to 5°N as a function of longitude. The 95% confidence interval is shown for MJO events occurred during the non–El Niño periods (gray) and prior to El Niño (red).

FINESST grant (80NSSC21K1590). Comments from three anonymous reviewers helped improve the manuscript.

Data availability statement. The data used in this paper were obtained from the Remote Sensing Systems (CCMP V2.0; www.remss.com), the NASA/Goddard Space Flight Center and archived at the NASA GES DISC online (TMPA data; https://disc.gsfc.nasa.gov/datasets/TRMM_3B42_Daily_7/summary), the NOAA/OAR/ESRL PSL (High Resolution SST; https://psl.noaa.gov/) and the Climate Prediction Center (https://www.cpc.ncep.noaa.gov/data/indices/sstoi.indices). The MJO-LPT system database created by Kerns and Chen (2020) and used in this study is available online (http://orca.atmos.washington.edu/data/lpt).

REFERENCES

Anderson, S. P., R. A. Weller, and R. B. Lukas, 1996: Surface buoyancy forcing and the mixed layer of the western Pacific warm pool: Observations and 1D model results. *J. Climate*, **9**, 3056–3085, https://doi.org/10.1175/1520-0442(1996)009<3056:SBFATM>2.0.CO;2.

Atlas, R., J. Ardizzone, and R. N. Hoffman, 2008: Application of satellite surface wind data to ocean wind analysis. *Proc. SPIE*, **7087**, 70870B, https://doi.org/10.1117/12.795371.

Barnston, A. G., M. K. Tippett, M. L. L'Heureux, S. Li, and D. G. DeWitt, 2012: Skill of real-time seasonal ENSO model predictions during 2002–2011: Is our capability increasing? *Bull. Amer. Meteor. Soc.*, **93**, 631–651, https://doi.org/10.1175/BAMS-D-11-00111.1.

Bergman, J. W., H. H. Hendon, and K. M. Weickmann, 2001: Intraseasonal air–sea interactions at the onset of El Niño. *J. Climate*, **14**, 1702–1719, https://doi.org/10.1175/1520-0442(2001)014<1702:IASIAT>2.0.CO;2.

Bosc, C., T. Delcroix, and C. Maes, 2009: Barrier layer variability in the western Pacific warm pool from 2000 to 2007. *J. Geophys. Res.*, **114**, C06023, https://doi.org/10.1029/2008JC005187.

Brown, J. N., C. Langlais, and C. Maes, 2014: Zonal structure and variability of the western Pacific dynamic warm pool edge in CMIP5. *Climate Dyn.*, **42**, 3061–3076, https://doi.org/10.1007/s00382-013-1931-5.

Capotondi, A., and Coauthors, 2015: Understanding ENSO diversity. *Bull. Amer. Meteor. Soc.*, **96**, 921–938, https://doi.org/10.1175/BAMS-D-13-00117.1.

Chen, S. S., and R. A. Houze Jr., 1997a: Diurnal variation and lifecycle of deep convective systems over the tropical Pacific warm pool. *Quart. J. Roy. Meteor. Soc.*, **123**, 357–388, https://doi.org/10.1002/qj.49712353806.

——, and ——, 1997b: Interannual variability of deep convection over the tropical warm pool. *J. Geophys. Res.*, **102**, 25 783–25 795, https://doi.org/10.1029/97JD02238.

——, ——, and B. E. Mapes, 1996: Multiscale variability of deep convection in relation to large-scale circulation in TOGA COARE. *J. Atmos. Sci.*, **53**, 1380–1409, https://doi.org/10.1175/1520-0469(1996)053<1380:MVODCI>2.0.CO;2.

Chiodi, A. M., D. E. Harrison, and G. A. Vecchi, 2014: Subseasonal atmospheric variability and El Niño waveguide warming: Observed effects of the Madden–Julian Oscillation and westerly wind events. *J. Climate*, **27**, 3619–3642, https://doi.org/10.1175/JCLI-D-13-00547.1.

Clarke, A. J., J. Wang, and S. V. Gorder, 2000: A simple warm-pool displacement ENSO Model. *J. Phys. Oceanogr.*, **30**, 1679–1691, https://doi.org/10.1175/1520-0485(2000)030<1679:ASWPDE>2.0.CO;2.

Delcroix, T., and C. Hénin, 1991: Seasonal and interannual variations of sea surface salinity in the tropical Pacific Ocean. *J. Geophys. Res.*, **96**, 22 135–22 150, https://doi.org/10.1029/91JC02124.

Drushka, K., H. Bellenger, E. Guilyardi, M. Lengaigne, J. Vialard, and G. Madec, 2015: Processes driving intraseasonal displacements of the eastern edge of the warm pool: The contribution

Brought to you by NOAA Central Library | Unauthenticated | Downloaded 08/13/24 07:09 PM UTC

of westerly wind events. *Climate Dyn.*, **44**, 735–755, https://doi.org/10.1007/s00382-014-2297-z.

Fedorov, A. V., S. Hu, M. Lengaigne, and E. Guilyardi, 2015: The impact of westerly wind bursts and ocean initial state on the development, and diversity of El Niño events. *Climate Dyn.*, **44**, 1381–1401, https://doi.org/10.1007/s00382-014-2126-4.

Graham, N. E., and T. P. Barnett, 1987: Sea surface temperature, surface wind divergence, and convection over tropical oceans. *Science*, **238**, 657–659, https://doi.org/10.1126/science.238.4827.657.

Guilyardi, E., A. Wittenberg, A. Fedorov, M. Collins, C. Wang, A. Capotondi, G. J. van Oldenborgh, and T. Stockdale, 2009: Understanding El Niño in ocean–atmosphere general circulation models: Progress and challenges. *Bull. Amer. Meteor. Soc.*, **90**, 325–340, https://doi.org/10.1175/2008BAMS2387.1.

Hendon, H. H., B. Liebmann, and J. D. Glick, 1998: Oceanic Kelvin waves and the Madden–Julian oscillation. *J. Atmos. Sci.*, **55**, 88–101, https://doi.org/10.1175/1520-0469(1998)055<0088:OKWATM>2.0.CO;2.

——, M. C. Wheeler, and C. Zhang, 2007: Seasonal dependence of the MJO–ENSO relationship. *J. Climate*, **20**, 531–543, https://doi.org/10.1175/JCLI4003.1.

Houze, R. A., Jr., S. S. Chen, D. Kingsmill, Y. Serra, and S. E. Yuter, 2000: Convection over the Pacific warm pool in relation to the atmospheric Kelvin–Rossby wave. *J. Atmos. Sci.*, **57**, 3058–3089, https://doi.org/10.1175/1520-0469(2000)057<3058:COTPWP>2.0.CO;2.

Huffman, G. J., and Coauthors, 2007: The TRMM Multisatellite Precipitation Analysis (TMPA): Quasi-global, multiyear, combined-sensor precipitation estimates at fine scales. *J. Hydrometeor.*, **8**, 38–55, https://doi.org/10.1175/JHM560.1.

Jauregui, Y. R., and K. Takahashi, 2018: Simple physical-empirical model of the precipitation distribution based on a tropical sea surface temperature threshold and the effects of climate change. *Climate Dyn.*, **50**, 2217–2237, https://doi.org/10.1007/s00382-017-3745-3.

Judt, F., and S. S. Chen, 2014: A explosive convective cloud system and its environmental conditions in MJO initiation observed during DYNAMO. *J. Geophys. Res. Atmos.*, **119**, 2781–2795, https://doi.org/10.1002/2013JD021048.

Kerns, B. W., and S. S. Chen, 2016: Large-scale precipitation tracking and the MJO over the Maritime Continent and Indo-Pacific warm pool. *J. Geophys. Res. Atmos.*, **121**, 8755–8776, https://doi.org/10.1002/2015JD024661.

——, and ——, 2020: A 20-year climatology of Madden-Julian Oscillation convection: Large-scale precipitation tracking from TRMM-GPM rainfall. *J. Geophys. Res. Atmos.*, **125**, e2019JD032142, https://doi.org/10.1029/2019JD032142.

——, and ——, 2021: Impacts of precipitation-evaporation-salinity coupling on upper ocean stratification and momentum over the tropical Pacific prior to onset of the 2018 El Niño. *Ocean Modell.*, **168**, 101892, https://doi.org/10.1016/j.ocemod.2021.101892.

Kessler, W. S., 2002: Is ENSO a cycle or a series of events? *Geophys. Res. Lett.*, **29**, 2125, https://doi.org/10.1029/2002GL015924.

——, and R. Kleeman, 2000: Rectification of the Madden–Julian oscillation into the ENSO cycle. *J. Climate*, **13**, 3560–3575, https://doi.org/10.1175/1520-0442(2000)013<3560:ROTMJO>2.0.CO;2.

——, M. J. McPhaden, and K. M. Weickmann, 1995: Forcing of intraseasonal Kelvin waves in the equatorial Pacific. *J. Geophys. Res.*, **100**, 10 613–10 631, https://doi.org/10.1029/95JC00382.

Kug, J.-S., K.-P. Sooraj, T. Li, and F.-F. Jin, 2010: Precursors of the El Niño/La Niña onset and their interrelationship. *J. Geophys. Res.*, **115**, D05106, https://doi.org/10.1029/2009JD012861.

Latif, M., T. P. Barnett, M. A. Cane, M. Flügel, N. E. Graham, H. von Storch, J.-S. Xu, and S. E. Zebiak, 1994: A review of ENSO prediction studies. *Climate Dyn.*, **9**, 167–179, https://doi.org/10.1007/BF00208250.

Lau, K.-M., and P. H. Chan, 1988: Intraseasonal and interannual variations of tropical convection: A possible link between the 40–50 day oscillation and ENSO? *J. Atmos. Sci.*, **45**, 506–521, https://doi.org/10.1175/1520-0469(1988)045<0506:IAIVOT>2.0.CO;2.

Lengaigne, M., J. Boulanger, C. Menkes, S. Masson, G. Madec, and P. Delecluse, 2002: Ocean response to the March 1997 westerly wind event. *J. Geophys. Res.*, **107**, 8015, https://doi.org/10.1029/2001JC000841.

——, ——, ——, G. Madec, P. Delecluse, E. Guilyardi, and J. Slingo, 2003: The March 1997 westerly wind event and the onset of the 1997/98 El Niño: Understanding the role of the atmospheric response. *J. Climate*, **16**, 3330–3343, https://doi.org/10.1175/1520-0442(2003)016<3330:TMWWEA>2.0.CO;2.

L'Heureux, M. L., and Coauthors, 2017: Observing and predicting the 2015/16 El Niño. *Bull. Amer. Meteor. Soc.*, **98**, 1363–1382, https://doi.org/10.1175/BAMS-D-16-0009.1.

Lukas, R., and E. Lindstrom, 1991: The mixed layer of the western equatorial Pacific Ocean. *J. Geophys. Res.*, **96**, 3343–3357, https://doi.org/10.1029/90JC01951.

Madden, R. A., and P. R. Julian, 1971: Detection of a 40–50 day oscillation in the zonal wind in the tropical Pacific. *J. Atmos. Sci.*, **28**, 702–708, https://doi.org/10.1175/1520-0469(1971)028<0702:DOADOI>2.0.CO;2.

——, and ——, 1972: Description of global-scale circulation cells in the tropics with a 40–50 day period. *J. Atmos. Sci.*, **29**, 1109–1123, https://doi.org/10.1175/1520-0469(1972)029<1109:DOGSCC>2.0.CO;2.

Maes, C., and S. Belamari, 2011: On the impact of salinity barrier layer on the Pacific Ocean mean state and ENSO. *SOLA*, **7**, 97–100, https://doi.org/10.2151/sola.2011-025.

——, M. J. McPhaden, and D. Behringer, 2002: Signatures of salinity variability in tropical Pacific Ocean dynamic height anomalies. *J. Geophys. Res.*, **107**, 8012, https://doi.org/10.1029/2000JC000737.

——, J. Picaut, and S. Belamari, 2005: Importance of the salinity barrier layer for the buildup of El Niño. *J. Climate*, **18**, 104–118, https://doi.org/10.1175/JCLI-3214.1.

——, K. Ando, T. Delcroix, W. S. Kessler, M. J. McPhaden, and D. Roemmich, 2006: Observed correlation of surface salinity, temperature and barrier layer at the eastern edge of the western Pacific warm pool. *Geophys. Res. Lett.*, **33**, L06601, https://doi.org/10.1029/2005GL024772.

McPhaden, M. J., 1999: Genesis and evolution of the 1997-98 El Niño. *Science*, **283**, 950–954, https://doi.org/10.1126/science.283.5404.950.

——, 2004: Evolution of the 2002/03 El Niño. *Bull. Amer. Meteor. Soc.*, **85**, 677–696, https://doi.org/10.1175/BAMS-85-5-677.

——, 2012: A 21st century shift in the relationship between ENSO SST and warm water volume anomalies. *Geophys. Res. Lett.*, **39**, L09706, https://doi.org/10.1029/2012GL051826.

——, 2015: Playing hide and seek with El Niño. *Nat. Climate Change*, **5**, 791–795, https://doi.org/10.1038/nclimate2775.

——, and J. Picaut, 1990: El Niño-Southern Oscillation displacements of the western equatorial Pacific warm pool. *Science*, **250**, 1385–1388, https://doi.org/10.1126/science.250.4986.1385.

Brought to you by NOAA Central Library | Unauthenticated | Downloaded 08/13/24 07:09 PM UTC

——, and X. Yu, 1999: Equatorial waves and the 1997–98 El Niño. *Geophys. Res. Lett.*, **26**, 2961–2964, https://doi.org/10.1029/1999GL004901.

——, S. E. Zebiak, and M. H. Glantz, 2006a: ENSO as an integrating concept in Earth science. *Science*, **314**, 1740–1745, https://doi.org/10.1126/science.1132588.

——, X. Zhang, H. Hendon, and M. Wheeler, 2006b: Large scale dynamics and MJO forcing of ENSO variability. *Geophys. Res. Lett.*, **33**, L16702, https://doi.org/10.1029/2006GL026786.

Mechem, D. B., R. A. Houze Jr., and S. S. Chen, 2002: Layer inflow into precipitating convection over the western tropical Pacific. *Quart. J. Roy. Meteor. Soc.*, **128**, 1997–2030, https://doi.org/10.1256/003590002320603502.

——, S. S. Chen, and R. A. Houze Jr., 2006: Momentum transport processes in the stratiform regions of mesoscale convective systems over the western Pacific warm pool. *Quart. J. Roy. Meteor. Soc.*, **132A**, 709–736, https://doi.org/10.1256/qj.04.141.

Moore, A. M., and R. Kleeman, 1999: Stochastic forcing of ENSO by the intraseasonal oscillation. *J. Climate*, **12**, 1199–1220, https://doi.org/10.1175/1520-0442(1999)012<1199:SFOEBT>2.0.CO;2.

NOAA, 2016: El Niño and La Niña alert system. NOAA, accessed 10 December 2022, https://www.climate.gov/news-features/understanding-climate/el-ni%C3%B1o-and-la-ni%C3%B1a-alert-system.

Philander, S. G. H., T. Yamagata, and R. C. Pacanowski, 1984: Unstable air-sea interactions in the tropics. *J. Atmos. Sci.*, **41**, 604–613, https://doi.org/10.1175/1520-0469(1984)041<0604:UASIIT>2.0.CO;2.

Picaut, J., and T. Delcroix, 1995: Equatorial wave sequence associated with warm pool displacements during the 1986–1989 El Niño–La Niña. *J. Geophys. Res.*, **100**, 18 393–18 408, https://doi.org/10.1029/95JC01358.

——, F. Masia, and Y. Penhoat, 1997: An advective-reflective conceptual model for the oscillatory nature of the ENSO. *Science*, **277**, 663–666, https://doi.org/10.1126/science.277.5326.663.

——, M. Ioualalen, T. Delcroix, F. Masia, R. Murtugudde, and J. Vialard, 2001: The oceanic zone of convergence on the eastern edge of the Pacific warm pool: A synthesis of results and implications for El Niño–Southern Oscillation and biogeochemical phenomena. *J. Geophys. Res.*, **106**, 2363–2386, https://doi.org/10.1029/2000JC900141.

Puy, M., J. Vialard, M. Lengaigne, and E. Guilyardi, 2016: Modulation of equatorial Pacific westerly/easterly wind events by the Madden-Julian Oscillation and convectively coupled Rossby waves. *Climate Dyn.*, **46**, 2155–2178, https://doi.org/10.1007/s00382-015-2695-x.

Ralph, E. A., K. Bi, P. P. Niiler, and Y. du Penhoat, 1997: A Lagrangian description of the western equatorial Pacific response to the wind burst of December 1992: Heat advection in the warm pool. *J. Climate*, **10**, 1706–1721, https://doi.org/10.1175/1520-0442(1997)010<1706:ALDOTW>2.0.CO;2.

Reynolds, R. W., N. A. Rayner, T. M. Smith, D. C. Stokes, and W. Wang, 2002: An improved in situ and satellite SST analysis for climate. *J. Climate*, **15**, 1609–1625, https://doi.org/10.1175/1520-0442(2002)015<1609:AIISAS>2.0.CO;2.

——, T. M. Smith, C. Liu, D. B. Chelton, K. S. Casey, and M. G. Schlax, 2007: Daily high-resolution-blended analyses for sea surface temperature. *J. Climate*, **20**, 5473–5496, https://doi.org/10.1175/2007JCLI1824.1.

Rui, H., and B. Wang, 1990: Development characteristics and dynamic structure of tropical intraseasonal convection anomalies. *J. Atmos. Sci.*, **47**, 357–379, https://doi.org/10.1175/1520-0469(1990)047<0357:DCADSO>2.0.CO;2.

Savarin, A., and S. S. Chen, 2022a: Pathways to better prediction of the MJO: 1. Effects of model resolution and moist physics on atmospheric boundary layer and precipitation. *J. Adv. Model. Earth Syst.*, **14**, e2021MS002928, https://doi.org/10.1029/2021MS002928.

——, and ——, 2022b: Pathways to better prediction of the MJO: 2. Impacts of atmosphere-ocean coupling on the upper ocean and MJO propagation. *J. Adv. Model. Earth Syst.*, **14**, e2021MS002929, https://doi.org/10.1029/2021MS002929.

Shinoda, T., and H. H. Hendon, 2001: Upper-ocean heat budget in response to the Madden–Julian oscillation in the western equatorial Pacific. *J. Climate*, **14**, 4147–4165, https://doi.org/10.1175/1520-0442(2001)014<4147:UOHBIR>2.0.CO;2.

Singh, A., and T. Delcroix, 2013: Eastern and Central Pacific ENSO and their relationships to the recharge/discharge oscillator paradigm. *Deep Sea Res. I*, **82**, 32–43, https://doi.org/10.1016/j.dsr.2013.08.002.

Su, H., C. S. Bretherton, and S. S. Chen, 2000: Self-aggregation and large-scale control of tropical deep convection: A modeling study. *J. Atmos. Sci.*, **57**, 1797–1816, https://doi.org/10.1175/1520-0469(2000)057<1797:SAALSC>2.0.CO;2.

Suzuki, T., and K. Takeuchi, 2000: Response of equatorial Pacific mean temperature field to intraseasonal wind forcing. *J. Oceanogr.*, **56**, 485–494, https://doi.org/10.1023/A:1011140708962.

Vialard, J., and P. Delecluse, 1998: An OGCM study for the TOGA decade. Part II: Barrier-layer formation and variability. *J. Phys. Oceanogr.*, **28**, 1089–1106, https://doi.org/10.1175/1520-0485(1998)028<1089:AOSFTT>2.0.CO;2.

Wheeler, M. C., and H. H. Hendon, 2004: An all-season real-time multivariate MJO index: Development of an index for monitoring and prediction. *Mon. Wea. Rev.*, **132**, 1917–1932, https://doi.org/10.1175/1520-0493(2004)132<1917:AARMMI>2.0.CO;2.

Yoshida, K., 1959: A theory of the Cromwell Current (the Equatorial Undercurrent) and of the equatorial upwelling. *J. Oceanogr. Soc. Japan*, **15**, 159–170, https://doi.org/10.5928/kaiyou1942.15.159.

Zhang, C., 2005: Madden-Julian Oscillation. *Rev. Geophys.*, **43**, RG2003, https://doi.org/10.1029/2004RG000158.

——, 2013: Madden–Julian Oscillation: Bridging weather and climate. *Bull. Amer. Meteor. Soc.*, **94**, 1849–1870, https://doi.org/10.1175/BAMS-D-12-00026.1.

——, and J. Gottschalck, 2002: SST anomalies of ENSO and the Madden–Julian Oscillation in the equatorial Pacific. *J. Climate*, **15**, 2429–2445, https://doi.org/10.1175/1520-0442(2002)015<2429:SAOEAT>2.0.CO;2.

——, H. Hendon, W. Kessler, and A. Rosati, 2001: A workshop on the MJO and ENSO. *Bull. Amer. Meteor. Soc.*, **82**, 971–976.

Zhao, M., H. H. Hendon, O. Alves, G. Liu, and G. Wang, 2016: Weakened eastern Pacific El Niño predictability in the early twenty-first century. *J. Climate*, **29**, 6805–6822, https://doi.org/10.1175/JCLI-D-15-0876.1.

Brought to you by NOAA Central Library | Unauthenticated | Downloaded 08/13/24 07:09 PM UTC